12-10-2010

Mono-Dispersed Droplet Delivery in a Refrigerated Wind Tunnel

Kyle Hutchings

MONO-DISPERSED DROPLET DELIVERY IN A REFRIGERATED WIND TUNNEL

By

Kyle Hutchings

A Thesis
Submitted to the Faculty of
Mississippi State University
in Partial Fulfillment of the Requirements
for the Degree of Master of Science
in Aerospace Engineering
in the Department of Aerospace Engineering

Mississippi State, Mississippi

December 2010

MONO-DISPERSED DROPLET DELIVERY IN A REFRIGERATED WIND TUNNEL

By

Kyle Hutchings

Approved:

David S. Thompson Associate Professor of Aerospace Engineering (Major Professor)	J. Mark Janus Associate Professor of Aerospace Engineering (Committee Member and Graduate Coordinator)
Edward A. Luke Associate Professor of Computer Science and Engineering (Committee Member)	Sarah A. Rajala Dean of the James Worth Bagley College of Engineering

Name: Kyle Hutchings

Date of Degree: December 10, 2010

Institution: Mississippi State University

Major Field: Aerospace Engineering

Major Professor: David S. Thompson

Title of Study: MONO-DISPERSED DROPLET DELIVERY IN A REFRIGERATED WIND TUNNEL

Pages in Study: 64

Candidate for Degree of Master of Science

An aircraft may experience in-flight ice accretion and corresponding reductions in performance and control when the vehicle encounters clouds of super-cooled water droplets. In order to study anti-icing coatings, the EADS-IW Surface Engineering Group is building a refrigerated wind tunnel. Several variations of droplet delivery systems were explored to determine the most effective way to introduce mono-dispersed droplets into the wind tunnel. To investigate this flow, time-accurate, unsteady viscous flow simulations were performed using the Loci/CHEM flow solver with a multi-scale hybrid RANS/LES turbulence model. A Lagrangian droplet model was employed to simulate the movement of water droplets in the wind tunnel. It was determined that the droplet delivery system required pressure relief to properly orient the flow inside the droplet delivery tube. Additionally, a streamlined drop tube cross-section was demonstrated to reduce turbulence in the wake and decrease the variability in droplet trajectories in the test section.

DEDICATION

I would like to dedicate this to my Aunt Robin for her vision and foresight that has driven me to accomplish everything.

ACKNOWLEDGEMENTS

The support provided by EADS-North America and the contract monitor, Dr. Mark Fraser, which allowed me to work on this project, is gratefully acknowledged. Also, I must extend my gratitude to Dr. Dominik Raps and Mr. Stefan Jung at EADS-Innovation Works for without their support and vision, none of this would have been possible. I would also like to thank Dr. David Thompson for all of his hard work and guidance throughout my research experience. Without his expertise and advice, I would not be the engineer that I am today. I would also like to thank my committee members Dr. Ed Luke, and Dr. J. Mark Janus for their support and guidance along the way. I must especially thank Dr. Luke for all of his help regarding Loci/CHEM. And to Dr. Janus, thank you for reminding me why I wanted to study fluid mechanics with the simple question a few years ago. What makes a golf ball fly further?

I would also like to thank my parents and grandparents for their many years of support and guidance. Without them, I would surely not be the person that I am today. And I must say thanks to Allison for all of her support along the way; even though I believe she asked how many pages I had written more times than the final number of pages in this report. I must also thank God for putting me in such a wonderful place to fulfill my academic pursuits.

TABLE OF CONTENTS

LIST OF TABLES

LIST OF FIGURES

CHAPTER I

INTRODUCTION

1.1 Background

An aircraft may experience in-flight ice accretion and a corresponding reduction in performance and control when the vehicle encounters clouds of super-cooled water droplets. Federal Aviation Administration (FAA) Code of Federal Regulations (FAR) Part 25 Appendix C [1] addresses icing conditions that aircraft may experience in flight. Aircraft certified for ice protection must operate safely in the continuous and intermittent maximum icing conditions specified in Appendix C. Aircraft that are certified with ice protection systems generally employ one of three types of mechanical deicing systems [2]: pneumatic, electro-mechanical expulsion, or thermal deicing systems. Pneumatic deicing boots are rubber bladders attached to the leading edge of the wing and, when inflated, break ice off the surface of the boot. Similarly, electro-mechanical systems use mechanical vibrations to break the ice off of critical surfaces. Another variant of an electro-mechanical system, known as a weeping wing, secretes a chemical coating to cover these critical surfaces to prevent ice accretion. Thermal systems use either a series of flexible coils or bleed air from the engine to apply heat to critical surfaces thereby melting any accreted ice.

The tragic accidents involving American Eagle Flight 4184 [3] in October 1994 near Roselawn, IN and Comair Flight 3272 [4] in January 1997 near Monroe, MI prompted extensive research into aircraft icing prevention. Most of the resulting research

focused on super-cooled large droplet (SLD) icing conditions that were most likely the cause of both accidents. Although both aircraft were equipped with pneumatic deicing boots, the presence of SLD ice and warm ambient temperatures allowed significant runback, which caused ice accretion to occur behind the deicing boot on unprotected surfaces of the wing.

The European Aeronautics Defence and Space Company Innovation Works (EADS-IW) Surface Engineering Group is exploring passive deicing systems, such as anti-icing coatings, to prohibit ice accretion on aircraft surfaces. Unlike active systems, passive systems seek to prevent ice accretion instead of attempting to remove ice after formation. The circumstances of the Comair Flight 3272 accident show that ice may accrete rapidly and that ice formation on unprotected surfaces may prove unrecoverable for the pilots. A passive system would protect all surfaces during flight, which would reduce the possibility of ice formation.

The von Karman Institute for Fluid Dynamics (VKI) designed an icing tunnel for EADS-IW [5]. The icing tunnel is a low speed, closed loop system dedicated to studying the effects of in-flight aircraft icing. Figure 1.1 shows a schematic top view and cross sectional areas of the icing tunnel. Figure 1.2 shows a schematic side view of the test section side of the icing tunnel.

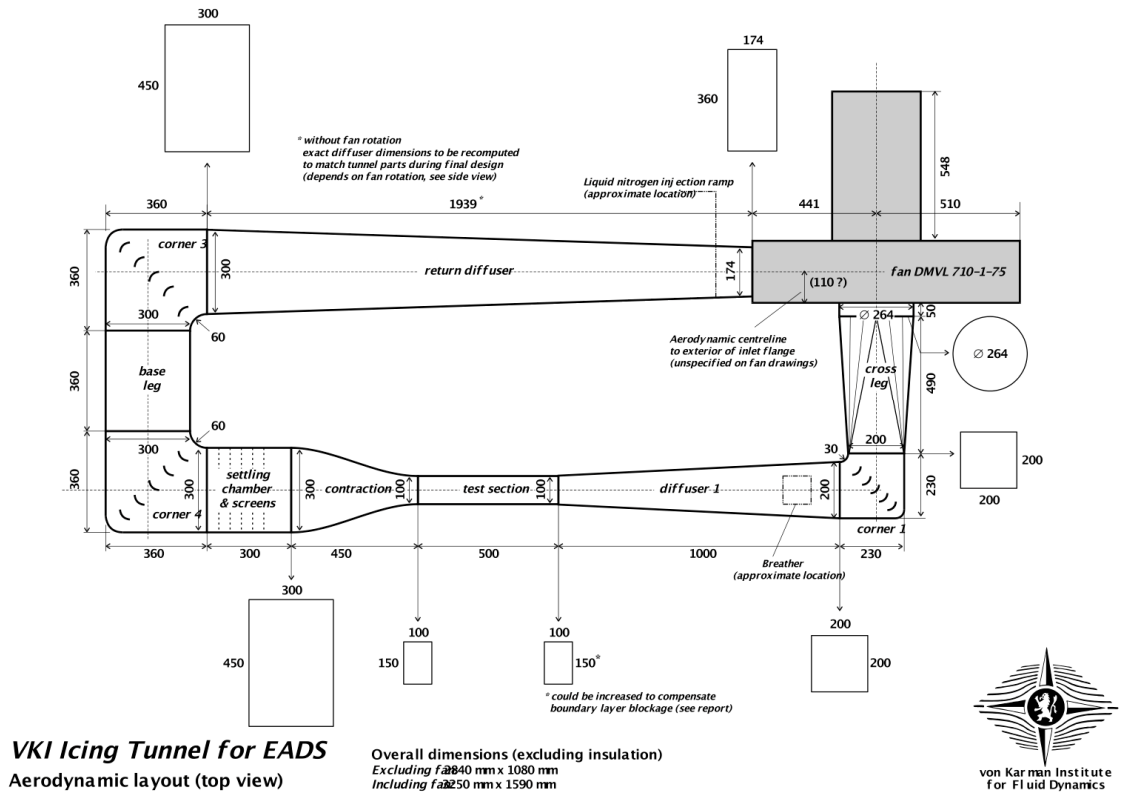

Figure 1.1 Schematic Top View of the VKI Icing Tunnel Designed for EADS-IW.

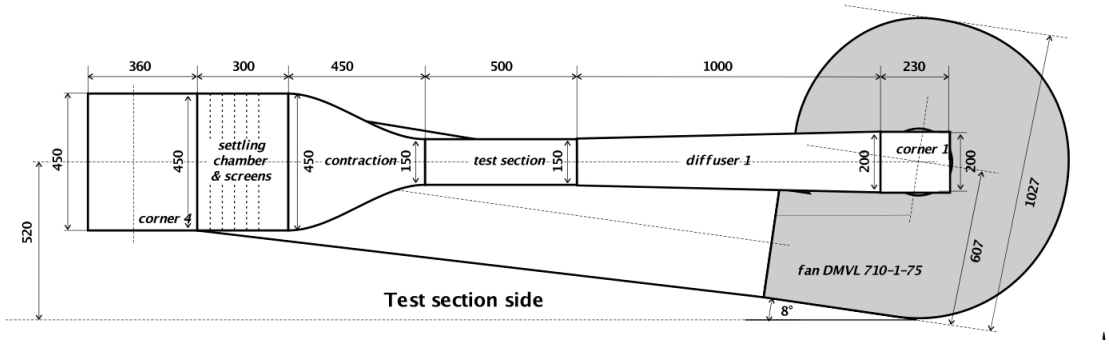

Figure 1.2 Schematic Side View of the EADS-IW Icing Tunnel.

The EADS-IW team desires to introduce mono-dispersed water droplets into the wind tunnel flow and have them impact a specimen located in the test section. The proposed system for introducing the droplets into the flow is shown in Figure 1.3, where the black arrows represent the direction of flow, the blue circles represent the water

droplets, and the grey cylinder represents the droplet delivery device referred to as the drop tube. This drop tube is intended to introduce the droplets into the flow upstream of the test specimen and to ensure that the droplets impact the test specimen. Figure 1.4 shows the approximate location of the proposed drop tube, which is colored red for clarity. This drop tube is not restricted to a circular cross section and may have any shape that facilitates delivery of the droplets so they impact the test specimen.

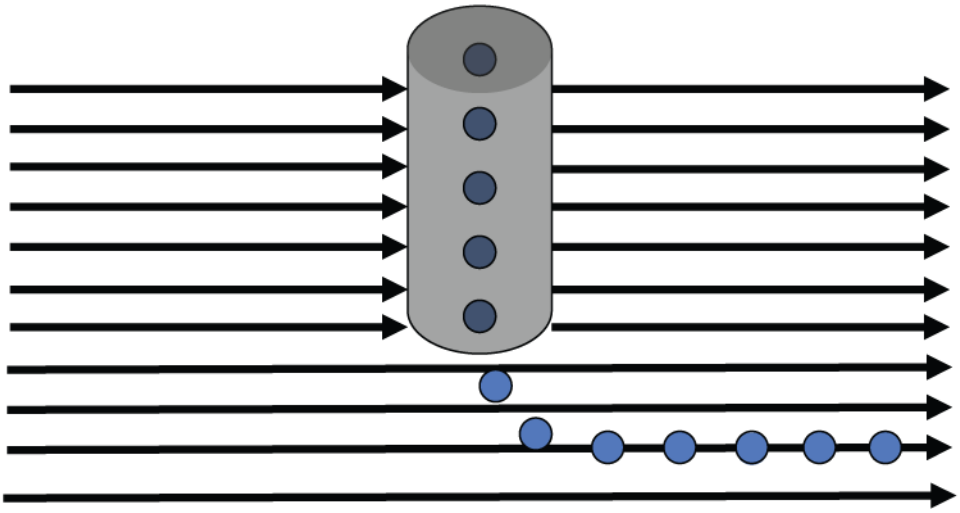

Figure 1.3 Initial Concept for Drop Tube.

Figure 1.4 Approximate Location of Drop Tube in Settling Chamber.

1.2 Primary Contributions

The primary contributions of this research include:

1. Validation of a drop tube design to introduce super-cooled liquid water droplets into the wind tunnel flow: The proposed design introduces a slot on the downstream side of a circular tube, which is an extension of the droplet creation device. This slot serves as a form of pressure relief that ensures that air flows through the cylindrical tube in the proper direction. Figure 1.5 shows the pressure relief slot and Figure 1.6 shows the exit of the drop tube where droplets enter the tunnel flow.

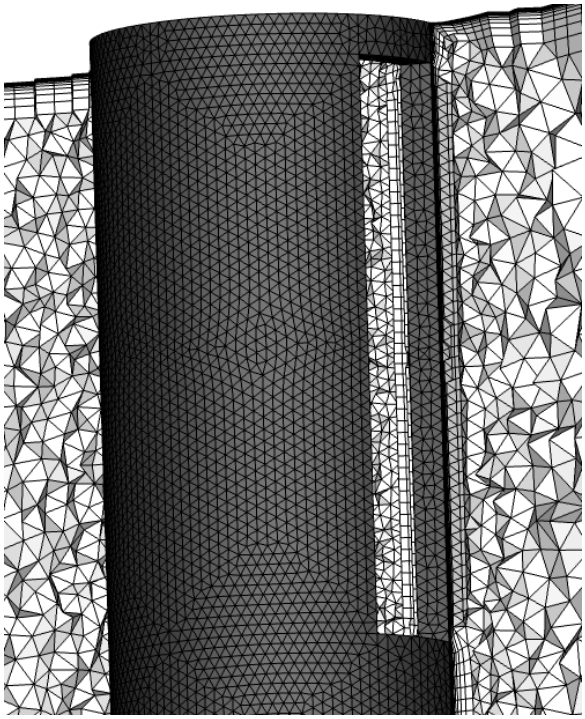

Figure 1.5 Pressure Relief Slot Location on the Downstream Side of the Drop Tube.

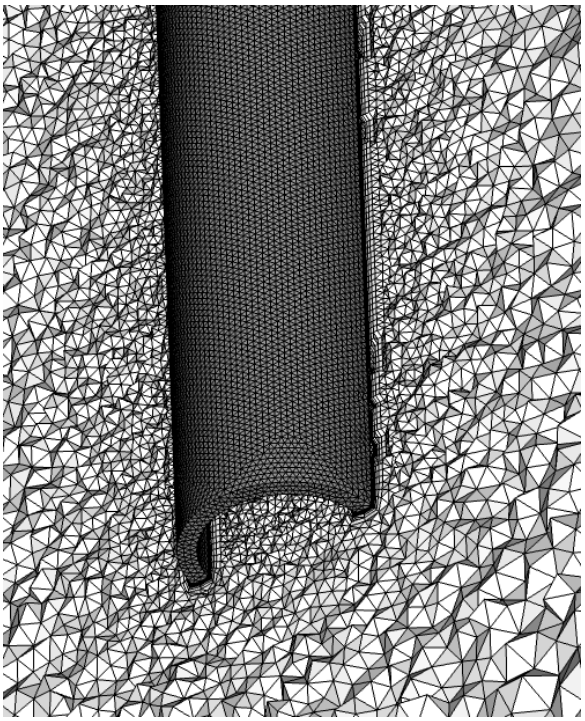

Figure 1.6 Exit of Drop Tube where Droplets Are Introduced to the Flow.

2. Reduction of wake effects on droplet delivery: Another component of this research was dedicated to analyzing the unsteady wake created by the drop tube. A hybrid geometry was introduced that combined a cylinder at the top of the wind tunnel and an airfoil-shaped collar around the lower portion of the tube. The cylindrical cross section allowed easy incorporation of the pressure relief slot while the airfoil collar introduced a more streamlined geometry in critical regions of the flow. Three different airfoil sections were tested as possible cross sectional geometries for this hybrid drop tube. Figure 1.7 shows a cut through view of each of the proposed hybrid droplet injection tube designs, which are fitted with collars based on NACA0020, NACA0030, and NACA0040 cross sections.

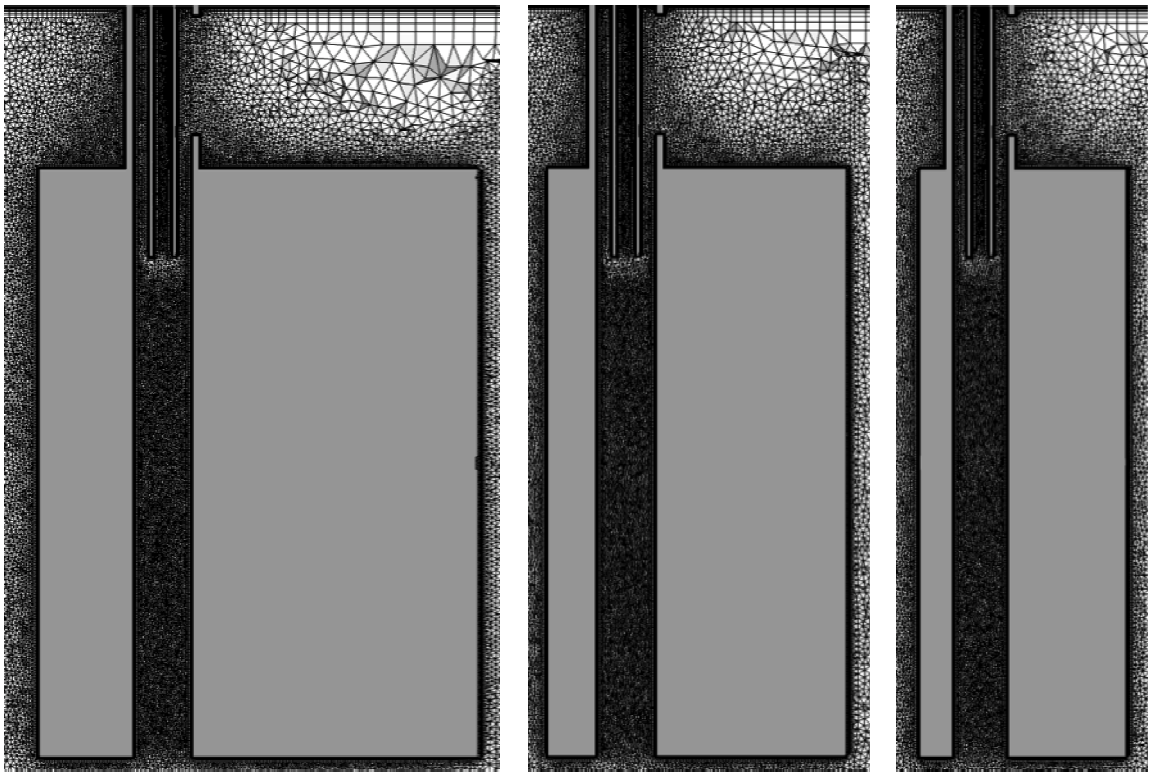

Figure 1.7 Left: NACA0020, Middle: NACA0030, Right: NACA0040.

1.3 Outline of Thesis

A literature review was performed to examine several important aspects of the present research. A survey of existing refrigerated wind tunnels was performed to document some of the current capabilities and features of wind tunnels dedicated to aircraft icing research. Since the present work models droplet trajectories in the wind tunnel to study their behavior, Eulerian and Lagrangian particle simulation methods are examined to determine which method might provide the most accurate simulations of the particle behavior. The next section focuses on the agreement between experimental and computational results, the accuracy of turbulence models, and the need for hybrid turbulence models. Since the results of the present study are based upon numerical

calculations of the flow in the wind tunnel, the next section focuses on the typical errors associated with numerical simulations. This section also explores mesh quality and mesh convergence as precautionary measures to avoid errors in simulations.

The general geometric design of the EADS-IW icing tunnel is then considered. This discussion covers the dimensions of the tunnel as provided by the schematic shown in Figure 1.1. The section also describes the drop tube geometry and the rationale behind the multiple cross-section designs. The next section provides general information about the computational methods used to simulate the flow through the wind tunnel. A general description of SolidMesh [6], the mesh generation tool used to create the discrete computational domain, is included. Finally, a brief overview of the Loci/CHEM [7] code covers the fundamentals of the numerical fluid dynamics calculations.

The results of the present work are then discussed. Within this section, the general description of the problem including the features of the mesh generation process and the boundary conditions that drive the numerical simulation are discussed. The next section deals with the design of the cylindrical drop tube and includes the time step size calculation, mesh convergence statistics, as well as droplet trajectory performance. The final section of results covers the alternate drop tube designs and compares their performance with the cylindrical drop tube.

CHAPTER II

LITERATURE REVIEW

2.1 Existing Refrigerated Wind Tunnels

There are several refrigerated wind tunnels of varying size and capabilities throughout the world. These tunnels include but are not limited to the tunnels at NASA Glenn, Boeing, the Canadian National Research Council, and the Italian Aerospace Research Centre. The Icing Research Tunnel (IRT) at NASA Glenn [8] is a closed loop refrigerated wind tunnel that simulates atmospheric conditions as low as -25^{o}F. The tunnel produces a velocity in the test section between 50 and 350 knots. The test section of the IRT is six feet tall, nine feet wide, and 20 feet long. A turntable in the test section rotates 20 degrees in either direction to simulate a variety of pitch conditions for the test specimen. Eight spray bars are used to produce a droplet cloud five feet tall and six feet wide. The cloud varies in liquid water content (LWC) from 0.5 to 2.5 g/m^3 of super-cooled droplets ranging from 15 to 50 microns in diameter.

The Boeing Research Aero-Icing Tunnel (BRAIT) [9] has a test section that is four feet tall by six feet wide and operates between -45^{o}F and 100^{o}F with airspeeds up to 250 knots. External turntables mounted about a horizontal axis allow rotation of the test specimen to simulate various angles of attack during flight. This facility also employs a spray bar system to generate droplet clouds three feet high by four feet wide. The cloud LWC varies from 0.25 to 2.5 g/m^3 consisting of droplets ranging from 15 to 40 microns in diameter.

The Extreme Icing Environment (EXTICE) research project utilizes the Italian Aerospace Research Center (CIRA) Icing Wind Tunnel (IWT) [10] to perform testing under natural icing conditions up to altitudes of 7000*m*. The tunnel operates over a temperature range between -40^{o}C and 35^{o}C at airspeeds up to Mach 0.7. The tunnel offers four different test sections to accommodate a variety of test specimens. The smallest of these test sections is 1.15 meters tall by 2.35*m* wide and the largest test section is 3.6*m* tall by 2.35*m* wide. A turntable rotates the test specimen 45 degrees about a horizontal axis to simulate various pitch angles typical of aircraft flight conditions. This tunnel also uses a modular nozzle, spray bar system to create a droplet cloud in the test section. Water and compressed air are fed through nozzles on 20 spray bars located 18*m* upstream of the test section. This system produces clouds made of water droplets ranging from five to 300 microns in diameter and LWC up to 4.0g/m^3. This system is capable of generating the conditions specified by the regulations of FAR Part 25 Appendix C as well as SLD conditions.

The Canadian National Research Institute for Aerospace Research (NRC Aerospace) Altitude Icing Wind Tunnel (AIWT) [11] is another tunnel dedicated to studying the effects of icing under realistic flight conditions. The test section is 57*cm* tall by 57*cm* wide and 183*cm* long. The tunnel operates at airspeeds up to 194 knots with a temperature range of -35 ^{o}C to 40^{o}C. An insert may be added to reduce the height of the test section to 30*cm* and increase the maximum airspeed to 320 knots. Like the CIRA IWT, this tunnel is capable of replicating flight conditions up to seven kilometers. The droplet cloud ranges in LWC from 0.1 to 3.0g/m^3 with droplets ranging between eight and 120 microns in diameter. The NRC does not specify the method of droplet

introduction, but the specification of LWC in the droplet cloud indicates some form of droplet spray as opposed to mono-dispersed droplets.

Existing refrigerated wind tunnels are capable of producing icing conditions specified by the regulations in FAR Part 25 Appendix C. These regulations do not currently cover SLD icing conditions although the CIRA IWT and NRC AIWT are capable of producing large droplets consistent with natural SLD conditions. Each of the reviewed refrigerated tunnels employ a series of spray bars to generate a cloud of particles. Typically, water is pushed through these spray bars by pressurized air and out of nozzles producing a mist of water droplets in the chilled air. The CIRA IWT and NRC AIWT tunnels also provide a range of altitudes whereas the NASA Glenn IRT and BRAIT operate at sea level conditions. Since the studies focus on in-flight ice accretion instead of ground icing, altitude simulation may provide more realistic test conditions.

2.2 Numerical Simulation Techniques

There are three ways to introduce turbulent flow physics within numerical simulations: direct numerical simulations (DNS), large eddy simulations (LES), and Reynolds Averaged Navier-Stokes (RANS) simulations. The objective of the DNS approach is to simulate the complete statistical range of turbulent fluctuations at all relevant length and time scales. Hirsh [12] notes that integrating the Navier-Stokes (NS) equations in time requires temporal and spatial resolution small enough to resolve the smallest eddies and concludes that solving the Navier-Stokes equations for turbulent flows using DNS requires on the order of Re^3 arithmetic operations, where Re is the Reynolds number. Thus, due to the extreme computational requirements, DNS is not

currently a viable option for full-scale geometries and some type of turbulence modeling is required.

A somewhat less computationally intensive approach is LES, which attempts to compute the turbulent fluctuations of the large-scale eddies and model fluctuations in the smallest scales, sometimes referred to as the sub-grid scales (SGS). Hirsh shows that the number of arithmetic operations required for LES is on the order of $Re^{9/4}$. Although the LES methods require significantly less computational resources than DNS methods, these models suffer computationally by requiring highly refined, isotropic grids at the sub-grid level. Spalart [13] projected that three or four decades of advancements in technology might produce the computing resources required for performing full three-dimensional LES for complete aircraft configurations.

RANS methods are the most commonly used approach for solving the Navier-Stokes equations. These methods rely on empirical or semi-empirical models for the effects of the turbulent fluctuations, since RANS averages the unsteady quantities over time. Brueur [14] concludes that RANS models only produce marginal results for complex turbulent flows. Nichols and Nelson [15] note that typical RANS models suffer because they predict excessive eddy viscosity and tend to over-damp the motion of the fluid. In regions of strong vortices and unsteadiness, this results in under prediction of the motion of the fluid.

2.2.1 Turbulence Modeling for Flow around a Cylinder

From many years of experimental studies, it is well known that laminar flow separation generates a turbulent unsteady wake downstream of a cylinder. Thus, the flow around a cylinder is fundamentally an unsteady problem, which requires computationally

intensive approaches to simulate. Tutar *et al*. [16] support this idea by stating that, while the flow around a cylinder is a common application, it presents numerous problems from a simulation perspective. They also suggest that, although turbulence increases dramatically at higher Reynolds numbers, the low Reynolds number conditions may also require models to resolve the transition from laminar to turbulent flow. Their work presents finite element solutions to flow around a two-dimensional circular cylinder using various turbulence models to determine if turbulence models affect the accuracy of the simulation, as determined by comparison to experimental results. Tutar *et al*. [16] studied standard k-ε, the Re-Normalization Group (RNG) k-ε, and LES methods of predicting turbulent flow. They concluded that the standard and modified k-ε models tended to under predict significant flow characteristics in the turbulent regions. They suggest that this may be the result of numerical dissipation introduced to the simulation in regions where vortex shedding occurs. They also note that LES predicted stronger, less elongated vortices than the experimental data presents, which they suggest may lead to the over prediction of the vortex motion. This may be a function of the two-dimensional geometry that the authors used to simulate the flow field. Vortex shedding is fundamentally a complex three-dimensional problem, and simplifications in two dimensions might lead to some of the inaccuracies predicted by this approach.

Celik [17] notes that LES simulations were too computationally expensive to be performed on sufficiently refined meshes. However, Breuer [14] suggests that the concept behind LES simulations might offer a suitable means for solving for the flow around bluff bodies. Breuer adds that LES simulations were generally performed on Cartesian or spectral grids; but curvilinear body-fitted grids are needed to solve more complex problems.

2.2.2 Hybrid Turbulence Modeling Approaches

In an attempt to more accurately resolve large-scale turbulent flow features, Spalart [13] developed a hybrid RANS/LES method which he coined detached-eddy simulation (DES). DES combines Smagorinski's [18] LES model with Spalart's standard one-equation turbulence model [19]. Fundamentally, DES computes the fluctuations due to large eddies directly and transitions to RANS to model small-scale turbulence in regions where the grid scale is smaller than the distance to the wall:

$$\bar{d} = \min(d, C_{DES} \cdot L_g) \tag{2.1}$$

with a DES coefficient, C_{DES}=0.65 and local grid spacing, L_g=max(dx,dy,dz). The distance to the wall $\bar{d}$ replaces the wall distance in the eddy destruction term of Spalart's standard model. This modification serves as the filtering function between RANS and LES. This method does not include any turbulent length scale consideration when filtering between the models.

Travin [20] describes the DES method as a combination of RANS in the boundary layer with LES in the separated regions. The turbulence model maintains full control of the solution in the RANS regions of the simulation; however, these models are applied only in regions where RANS assumptions are well justified. The regions of flow separation use the LES method to resolve the large eddies. Travin applied DES to flow past a circular cylinder. Although the DES results did not match experimental results, they matched the features of the separated flow such as the pressure on the downstream side of the cylinder better than unsteady RANS methods. Roy *et al*. [21] compared DES with steady-state RANS models and determined that DES produced better predictions of wake velocity and turbulent fluctuations.

Nichols and Nelson [14] present a hybrid RANS/LES method that filters between Menter's [22] SST model and an LES method [7]. They refer to their method as a multi-scale (MS) model because it relies upon a turbulent length scale to transition between LES and RANS. The filtering function controlling the transition must fundamentally not harm the accuracy of the solution or the performance of the models. Such a resulting hybrid model should transition from LES to RANS when the grid scale no longer resolves the turbulence scales. The multi-scale model is the method employed in the present work. Nichols and Nelson [15] examined both DES and multi-scale hybrid RANS/LES to determine the most accurate approach. In general, they found the DES to transition from RANS to LES abruptly, whereas the multi-scale method performed well on the test cases observed. Their findings concluded by showing that the DES model did not sufficiently predict the motion of the flow in regions outside of the boundary layer.

2.2.3 Agreement between Experimental and Numerical Models

Experimental studies show that flow around a cylinder in the subcritical Reynolds number range generates a laminar boundary layer that separates at $\phi = 80^o$ [23]. Celik [17] notes several typical traits of subcritical flow around cylindrical bluff bodies as presented by prior experimental studies. His research supports Bloor's [23] analysis that suggests flow separation occurs at $\phi = 80^o$. Celik also concludes that RANS simulations tend to agree well with experimental solutions up to and including the point of separation. RANS solutions do not, however, provide consistent agreement with experimental results beyond the separation point since these methods average turbulent fluctuations over time. Celik also notes that the presence of the vortices fundamentally affects the flow in this region. Holloway *et al*. [24] further suggest that turbulence models used with RANS

solutions are incapable of simulating the effects of transition. The authors also note that current models may only be applicable to fully turbulent flow due to this inability to resolve this transition phase and the conditions are only exactly satisfied as the Reynolds number approaches infinity. Tutar *et al*. [16] studied the application of several turbulence models to this problem and showed that LES accurately predicted separation, especially when compared to the standard *k*-ε models, which suggested that this separation occurs near 90^{o}. They state that this may indicate the ability of LES to more adequately model the free shear layer flow when compared to the RANS models.

Celik [17] adds that other factors such as surface roughness and adverse pressure gradient also greatly affect the flow; but like the presence of the vortices, RANS simulations largely ignore these factors. Breuer [25] suggests that turbulent flow around a cylinder is not only a function of Reynolds numbers, but rather a more complicated solution dependent on the aspect ratio of the cylinder, blockage ratio of the wind or water tunnel, downstream conditions, surface roughness of the cylinder, free stream turbulence, and Mach number. This complicated situation may explain the wide variety in the experimental and numerical predictions of the transition to turbulent flow.

2.3 Eulerian and Lagrangian Droplet Simulation

Both Eulerian and Lagrangian droplet simulation techniques couple particle motion and fluid motion for time-accurate simulations. The Eulerian method treats droplets as a continuum and couples particle concentration equations with the flow equations [26]. This method is appropriate for tracking collections of droplets or multi-fluid interactions. Zheng and Chen contend that the Eulerian method is particularly effective at predicting concentration distributions of particles in enclosed environments

[27]. Lagrangian droplet simulations model a discrete number of droplets interacting with the fluid. Since each droplet in the field is modeled individually, the motion of individual droplets is resolved using this technique [28]. The Lagrangian method is most effective at predicting dispersion patterns of large numbers of particles. [27].

2.4 Typical Errors in Numerical Simulations

Brueur [14] examines the errors associated with numerical simulations and divides these errors into three distinct subsets: modeling error, discretization error, and convergence error. Modeling error addressed the difference between the physics and the exact solution of the mathematical model. Discretization error refers to the difference between the exact mathematical solution and the solution of the discrete equations used in the numerical simulation. Lastly, the convergence error describes the difference between the iterated solution and the exact solution of the discrete solution. The next section discusses both mesh quality and mesh refinement and their impacts on solution error. It should be noted that improving mesh quality does not guarantee improvement in solution accuracy; however, it may identify possible error sources such as inverted and sliver elements.

2.4.1 Mesh Quality

Simply stated, a high quality mesh is one that produces an acceptable answer from a numerical simulation. Knupp [29] states "mesh quality concerns the characteristics of a mesh that permit a particular numerical PDE simulation to be efficiently performed, with fidelity to the underlying physics, and with the accuracy required for the problem." Quantifying mesh quality presents problems since most quality metrics are designed with

specific problem parameters in mind. Criteria for grid quality are generally based on geometric quantities such as angle, shape, twist, and aspect ratio of cells. Mavriplis et al. [30] add element type and orthogonality for structured or semi-structured grids to the list of possible quality metrics. While these quantities are easily obtainable, they do not provide any direct connection to the physical problem that is being simulated.

Mavriplis et al. [30] alludes to the use of varying types of elements within a given mesh and states that the associated grid quality metrics may differ substantially for different types of meshes. We can classify meshes in one of two distinct categories: structured and unstructured. Luke et al. [31] acknowledge that structured meshes tend to produce the best solutions when the elements are orthogonal and the cells are smoothly stretched. As they also note that this is a result of the coupling between stretching and orthogonality for structured curvilinear grids. The term unstructured mesh describes a much more loosely defined category since these meshes may include all-tetrahedral elements, all-hexahedral elements, or a hybrid mix of tetrahedral, prismatic, and pyramidal elements. Mavriplis et al. [30] point out that a precise quantification of the effects on solution accuracy of using fully tetrahedral elements versus hybrid tetrahedral-prismatic meshes is still lacking. Most common unstructured meshes employ a mix of element types to ensure that the boundary-layer region consists of smoothly stretched, orthogonal elements. They continue by stating that unstructured meshes consisting of all hexahedral elements may reduce small angle elements by stretching the grid in multiple directions, thus producing more accurate solutions for separated flow conditions.

Knupp [29] reiterates that the term mesh quality metric is somewhat of a misnomer since the metrics only measure element or local properties. He points out that

valid uses of such metrics include automatic defect detection, assessment of mesh generation results coupled with engineering judgment, non-adaptive calculations, and *a priori* mesh improvement methods. Automatic defect detection refers to the application of metrics during the initial mesh generation process to ensure that small angles and inverted elements are removed from the final mesh. Similarly *a priori* mesh improvement employs metrics to improve local element quality through the use of edge swapping and node insertion techniques. This local quality enhancement produces the highest quality elements locally, which in theory produces a higher quality global mesh.

2.4.2 Mesh Convergence

The process of determining mesh convergence aims to ensure that the numerical simulation is not adversely affected by the element structure or refinement of the mesh. Salas [32] notes that mesh convergence is an important process in verifying that discrete numerical solutions are valid representations of the governing partial differential equations describing the phenomenon under investigation. Mavriplis et al. [29] add that the principle concept of mesh convergence states that, as the mesh resolution is increased in all areas of the domain, the discretization error in the solution should vanish and the discretized solution should gradually tend towards the continuous solution. Most mesh convergence studies attempt to obtain a consistent refinement through several levels of refinement. For a structured mesh, consistent refinement is a relatively simple procedure since neighboring cells can be divided similarly throughout the mesh. Similar refinement techniques exist for two-dimensional unstructured meshes, which simply divide each element. Refinement of general unstructured meshes in three dimensions proves more

difficult since most unstructured mesh generation techniques produce interior elements in a somewhat random order.

Thomas et al. [33] state that a consistent refinement satisfies the condition that the characteristic distance across cells decreases consistently with increase of total number of degrees of freedom, N. The characteristic distance should tend to zero as $N^{-1/d}$ where d is the number of spatial dimensions. Therefore, changing the characteristic distance by a factor of $2^{-1/3}$ roughly doubles the number of elements in the mesh. Similarly, changing the characteristic distance by a factor of $2^{1/3}$ reduces the number of elements in the mesh by a factor of 2. Consistent mesh refinement of unstructured grids is analogous to refinement families of structured grids.

Most consistent refinement techniques require three and prefer four levels of refinement to determine mesh convergence from the numerical simulations. Mavriplis et al. [30] suggest that this requirement presents a problem in terms of generating and employing sufficiently fine meshes. Employing Thomas et al.'s [33] consistent refinement technique on four meshes produces a finest mesh that is 16 times larger than the coarsest mesh. Since the coarsest mesh of the sequence must contain several million elements to fall within the asymptotic range, this level of refinement might well exceed current computational capabilities.

CHAPTER III

GEOMETRIC DESIGN

3.1 EADS-IW Icing Tunnel

The schematic drawings of the EADS-IW icing tunnel [5], which was designed by the von Karman Institute for Fluid Dynamics, are shown in figure 1.1. The EADS-IW Icing Tunnel is a closed loop wind tunnel. Flow leaving the fan passes through the return diffuser, corner 3, base leg, corner 4, settling chamber, contraction, test section, diffuser 1, corner 1, and cross leg closing the loop at the inlet to the fan. The settling chamber, contraction, test section, and diffuser 1 are the only elements included in the computational model employed here in order to reduce computational requirements. The length of the modeled segment of the icing tunnel is 2.25*m* from the inlet of the settling chamber to the outlet of diffuser 1. Figure 3.1 displays both the (a) VKI design, repeated here for convenience, and (b) the computational domain used in the present study.

Since the flow entering the settling chamber is exiting a ninety-degree turn in corner four, the VKI design calls for a series of screens to smooth and align the flow. The screens were not modeled in these simulations. The settling chamber is a 45*cm* tall by 30*cm* wide by 30*cm* long segment. The contraction smoothly reduces the cross-sectional area of the tunnel by a factor of nine. The exact shape of the contraction walls was not specified. Here, the bounding edges of the contraction were modeled as cubic splines. The test section is a constant area 10*cm* wide by 15*cm* tall by 50*cm* long segment of the tunnel. The diffuser is a 100*cm* long segment that expands to 20*cm* by 20*cm* and

includes a breather opening. The breather is important for any closed loop tunnel to maintain the proper pressure and temperature during continuous operation.

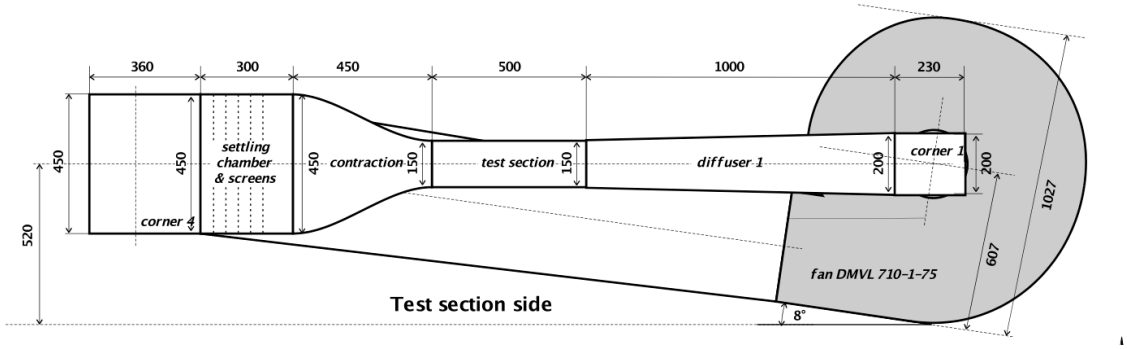

(a) VKI Design

(b) Computational Model

Figure 3.8 VKI Schematic and Computational Model Design.

3.2 Drop Tube Design

For the purpose of this study, the main feature of the icing tunnel is the drop tube. Computational geometries were produced with considerable refinement in the region around the drop tube. The region downstream of the drop tube was refined to capture the vortex shedding in its wake. Fluctuations in the downstream flow may potentially change the droplet trajectories and their impact locations on the test specimen.

Several variations in drop tube geometry were investigated to determine their effects on the downstream flow and resulting droplet trajectories. The baseline design was a 22.5*cm* long cylindrical tube with a 22*mm* outer diameter. The thickness of the drop tube walls was taken to be 2*mm* so that the inner diameter measures 18*mm*. This design evolved to include a pressure relief slot located on the downstream side of the tube near the upper wall of the settling chamber. Without some form of pressure relief, the longitudinal tunnel flow will entrain flow from the drop tube and produce a recirculating flow in the drop tube. This design is based on the observation that the pressure on the downstream side of the circular drop tube will be higher than the "freestream" pressure at the exit of the drop tube. The higher pressure at the slot will ensure that the flow enters the slot and proceeds downward inside the drop tube. The pressure relief slot, shown in figure 3.2, is located 2.5*mm* below the upper wall of the settling chamber and measures 36.3*mm* tall by 6.74*mm* wide. This size was selected so that the area of the slot is equal to the cross sectional area of the drop tube.

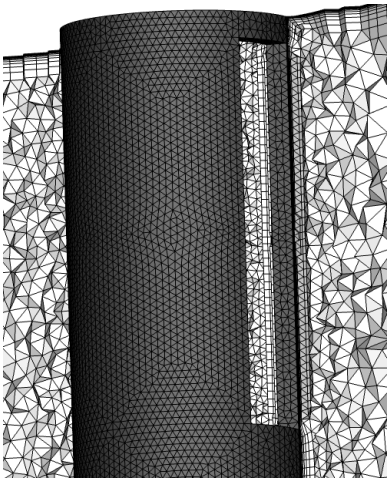

Figure 3.9 Pressure Relief Slot.

A concentrically mounted tube inside the slotted drop tube was introduced to produce a predominantly axial flow and reduce effects associated with the unsteady flow in the pressure relief slot. The exit of the inner tube is located 36.2*mm* lower than the bottom of the pressure relief slot to protect the droplets from the flow from the slot, which might adversely affect the droplet trajectories. Figure 3.3 shows the outline of the pressure relief slot and the inner tube, which is colored yellow for better visualization. The inner tube is a 7.5*cm* long cylindrical tube measuring 8*mm* in outer diameter. The walls of the inner tube were assumed to have a thickness of 1*mm* such that the inside diameter measures 6*mm*. The outer diameter of the inner tube was chosen to limit blockage inside the drop tube. For a given volume flow rate, an inner tube that occupies ½ of the area of the drop tube will increase the average velocity of the flow in that section of the drop tube by a factor of two.

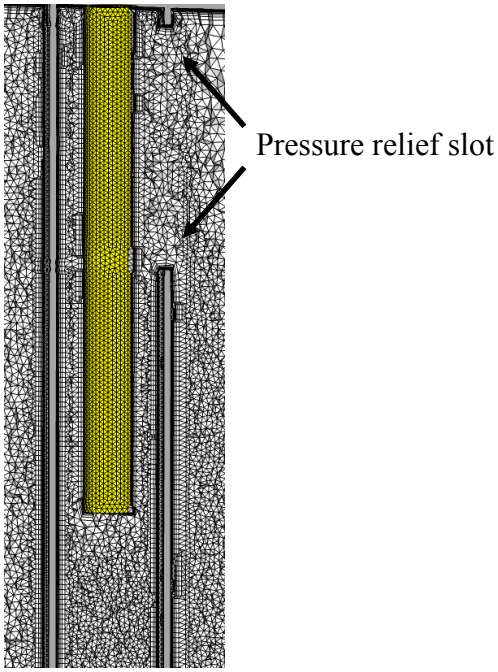

Figure 3.10 Outline of the Pressure Relief Slot and the Inner Tube.

This circular cylinder cross-section design may be preferable due to similarity to the droplet emitting apparatus, but it introduces unsteady artifacts to the flow. In order to reduce the fluctuations of the flow downstream of the drop tube, a series of airfoil shaped collars were introduced. NACA0020, NACA0030, and NACA0040 airfoils, shown in figure 1.7, were considered as possible cross sections to reduce the unsteadiness in the flow and its effects on the droplet trajectories.

CHAPTER IV

COMPUTATIONAL METHODS

4.1 Flow Solver

The numerical simulations were performed using Loci/CHEM, a reactive flow application based on the Loci framework introduced by Luke et al [7]. Loci is a rule-based system intended to automate the process of assembling numerical solver component, thereby reducing the complexity of the simulation process. The Loci/CHEM code is a set of rules that operates within the Loci framework that is specifically geared towards multiphase, chemically reacting flows. The code is a cell-centered, finite-volume scheme for computing flows on three-dimensional domains discretized using arbitrary polyhedral elements. The code is also capable of simulating non-reacting flows and includes droplet trajectory simulation capabilities.

For an arbitrary control volume, the general form the governing equations for three-dimensional flow with non-equilibrium chemistry and equilibrium internal energy may be written in the form of equation 4.1.

$$\frac{d}{dt}\int_{\Omega_C(t)} Q\, dV + \int_{\partial\Omega_C(t)} (F_i - F_v)\, dS = \int_{\Omega_C(t)} \dot{W}\, dV \tag{4.1}$$

The term Q represents the conservative state variables, F_i and F_v are the inviscid and viscous flux terms, respectively, and $\dot{W}$ is a source term [7] that accounts for production and destruction of species and turbulent quantities.

Time-accurate unsteady simulations were performed using the multi-scale, hybrid RANS/LES technique [14]. This approach uses LES to resolve large scale eddies in the flow, but switches to Menter's [21] SST turbulence model for the sub-grid scale. Menter [21] concludes that the SST model is the most accurate model for aerodynamic applications for its ability to predict pressure-induced separation and the associated viscous-inviscid interaction. A listing of a typical input vars file is included in the appendix.

4.2 Mesh Generation

The computational domain of the icing tunnel was modeled using an unstructured mesh generated using SolidMesh [6] and Marcum and Weatherill's [34] Advancing-Front/Local-Reconnection (AFLR) method. An unstructured surface mesh was generated on the bounding walls of the icing tunnel. This surface mesh serves as the initial front for the volume grid generation technique. The volume mesh was created using AFLR, which employs an advancing front technique to generate the positions of new points. The local reconnection portion of the method employs a min/max criterion to produce optimal quality for each cell in the domain. The min/max criterion seeks to minimize the maximum angle between any adjoining faces of a cell. The AFLR code is capable of generating hexahedral, pyramid, prismatic, and tetrahedral elements.

Since many turbulence models prefer elements that have faces parallel to the flow direction, the regions near the walls consist of stacked, semi-structured prismatic elements. The height of the initial prismatic elements is based on an estimated y^+ value of unity. The height of a cell grows proportionally to its distance from the wall. Once the height-length ratio reaches a predetermined value, the growth of these semi-structured

elements is terminated. The remainder of the domain is filled with tetrahedral elements created by the AFLR algorithm.

CHAPTER V

RESULTS

5.1 Problem Definition

Numerical trial and error demonstrated that fixing the total pressure at atmospheric pressure at the inflow and imposing a constant mass flow condition at the exit was the best combination of boundary conditions for this problem. The test section design Mach number M=0.2, a fixed total temperature of 268K, and test section cross-sectional area dictated a mass flow rate in the wind tunnel of 1.2967*kg/s*. Trial and error dictated the use of the PETSc [35] matrix inversion procedure instead of the Gauss-Seidel method. The PETSc routines used here employ the generalized minimal residual method (GMRES) [36] with a blocked incomplete lower-upper (ILU) preconditioner. In an effort to reduce negative effects of the boundary conditions on the flow simulation, an extruded segment was added to the exit of diffuser 1. The mesh in diffuser 1 was split into five sections and successively coarsened to promote diffusion of the solution. Diffusing the solution by coarsening the mesh in this region should have little effect on the motion of the flow in the test section and other critical segments of the wind tunnel.

As noted in the literature review, flow around a cylinder necessarily includes a transition from laminar to turbulent flow. However, predicting this transition using a RANS-based approach is not possible [24]. Therefore, the flow solution employed for this study assumed that the flow was fully turbulent throughout the domain. It is

suggested that the EADS-IW wind tunnel employ surface roughness near the stagnation line of the drop tube to ensure transition from laminar to turbulent flow.

Finally, water droplets are introduced into the computational domain via a circular injection surface with a diameter of 6*mm* for all of the geometry cases with or without the inner tube inside the drop tube. The droplets measure 60 microns in diameter and are injected at their terminal velocity of 0.11*m/s*. The droplet creation device emits droplets at a rate based upon the size of the droplet. For the 60 micron droplets, the emission rate is 80 droplets per minute. A droplet mass flow rate may be calculated based upon this predefined rate of droplets emission. The droplets are assumed to enter the domain at random locations in the entrance of the inner tube. It should be noted that, while this simulation will account for all possible droplet paths over time, it is not an exact simulation of the droplets emitted in the EADS-IW wind tunnel. The droplets simulated in this study cover all possible emission locations across the opening of the inner tube, whereas the real droplets are introduced individually across a much smaller portion of the inner tube opening. This will provide a conservative prediction for droplet trajectories and, at the same time, account for any statistical outliers. The prescribed droplet mass flow rate boundary condition will emit multiple droplets simultaneously, which is also contrary to the individual droplets released by the EADS-IW emitting apparatus. However, the droplets are not allowed to interact with each other.

5.2 Cylindrical Drop Tube

5.2.1 Definition of Temporal and Spatial Scales

Hirsch [12] notes that both the length scale and the time scale are crucial to accurately resolving the physical flow features. An estimate for the time scale required to

sufficiently resolve the flow is based on known flow characteristics. Using equation 5.2 with known values for the fluid velocity in the settling chamber, V=7.32m/s, the fluid density, ρ=1.317kg/m^3, diameter of the drop tube, d=0.022m, and the fluid viscosity, μ=1.70975e-5Ns/m^2, the Reynolds number is calculated to be Re=12404.

$$\mathrm{Re} = \frac{\rho V d}{\mu} \tag{5.2}$$

The Strouhal number is a dimensionless number that describes a periodic flow [37]. This dimensionless number measures the ratio of local acceleration to convective acceleration. There is much debate over the implementation and use of the Strouhal number in numerical simulations of flow past a circular cylinder since there is some variation found in the experimental results. While this variation may be explained by a number of factors in the experimental setup, the Strouhal number is generally approximated as 0.2 in sub-critical flow regimes [37]. Fey, König, and Eckelmann [37] investigated vortex shedding from a circular cylinder to determine the Reynolds number–Strouhal number relationship. They developed equation 5.3, a piecewise empirical formula to approximate the Strouhal number, which is valid for Reynolds numbers between 47 and $2\text{x}10^5$.

$$Sr = Sr^* + \frac{m}{\sqrt{\mathrm{Re}}} \tag{5.3}$$

The term Sr represents the Strouhal number and Sr^* and m are coefficients that depend on the Reynolds number. A graphical representation of their findings, shown in Figure 5.1, displays the variation in Strouhal numbers across a broad range of Reynolds numbers.

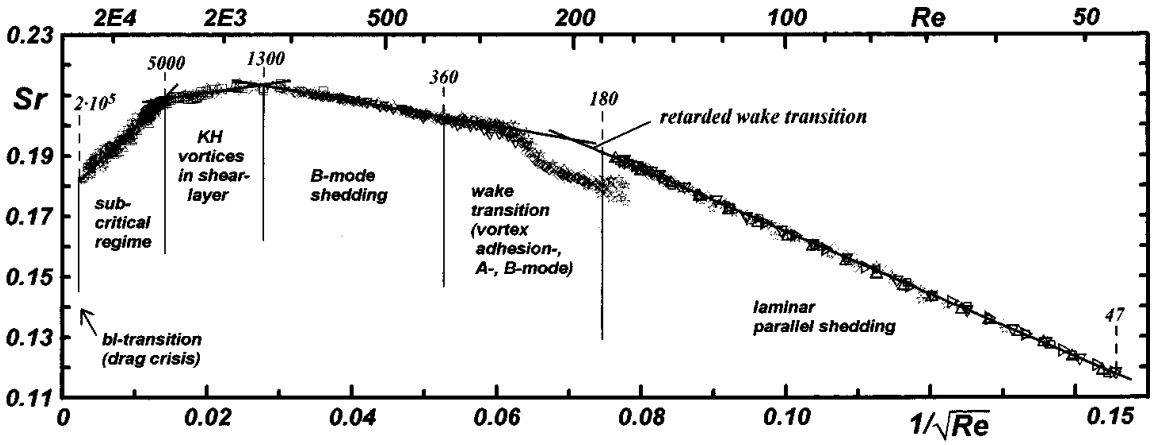

Figure 5.1 Strouhal Number–Reynolds Number Dependency in the Range $47<Re<2\text{x}10^5$. [37]

Table 5.1 Coefficients Sr^* and m for Various Reynolds Number Intervals. δr is the Estimated Error for the Straight-Line Approximation. [37]

Reynolds Number Range	Sr^*	m	δr	L/D	
47<Re<180	0.2684	-1.0356	0.0010	>50	laminar parallel shedding
180<Re<230	0.2437	-0.8607	0.0015	>50	wake transition
230<Re<240	0.4291	-3.6735	0.0015	>50	vortex adhesion
240<Re<360	depends on boundary conditions				A- and B- mode shedding
360<Re<1300	0.2257	-0.4402	0.0015	>50	B-Mode shedding
1300<Re<5000	0.2040	0.3364	0.0015	>50	Kelvin Helmholtz instability in shear layer
5000<Re<200000	0.1776	2.2023	0.0030	>15	subcritical regime

The Strouhal number only depends on the Reynolds number and the associated coefficients that can be obtained from Table 5.1. Since the Reynolds number of the flow of interest falls into the subcritical regime ($5000<Re<200{,}000$), Table 5.1 suggests using the coefficients $Sr^*=0.1776$ and $m=2.2023$ for the Strouhal number calculation. Using

these variables with Fey et al.'s equation 5.3, the Strouhal number is calculated to be St=0.197685, with an estimated error, δr=0.003. Knowing the Strouhal number, the periodic shedding frequency of the flow fluctuations may be obtained using equation 5.4

$$St = \frac{f\ d}{V} \tag{5.4}$$

where f is the frequency of shed vortices, d=0.022m is the characteristic length of the object present in the flow, and V=7.32m/s is the velocity of the flow. According to equation 5.4, the shedding frequency of the vortices for the cylindrical drop tube is 65.67Hz.

Travin [19] suggests sampling ten times the rate of the von Karman vortex shedding frequency to adequately resolve the shedding cycle. The present work employs 20 time steps per estimated vortex shedding cycle, or approximately 1313 samples per second. The amount of time between each numerical calculation is the inverse of the sampling frequency, which is calculated to be Δt=0.0007614s. Although strictly only valid for the circular cylinder cross sections, the time step was held constant for all cross-sectional designs of the drop tube, including the streamlined cross sections.

The length scale is the second crucial element required to resolve the motion of the flow. A mesh refinement study was performed to determine the effect of length scales on the flow solution. This mesh refinement study followed Thomas et al.'s [33] method for consistent refinement of unstructured meshes. The most refined mesh included a refined wake region downstream of the drop tube with element length scales of 1.64mm. Statistics for each of the three meshes are provided in table 5.2. The three levels of refinement are displayed in figure 5.2

Table 5.2 Mesh Statistics for the Mesh Refinement Study.

	Number of Nodes	Total Number of Elements	Number of Hex Elements	Number of Pyramid Elements	Number of Prismatic Elements	Number of Tetrahedral Elements
Coarse	1389124	4784485	2592	2648	1693090	3086155
Baseline	2389231	8844402	3052	2276	2610440	6228666
Refined	4231645	16671702	3744	2430	4130278	12535250

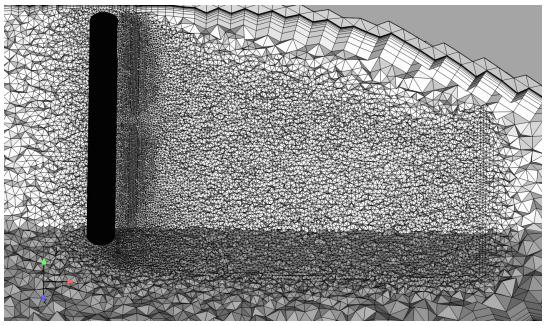

(a) Coarse Mesh

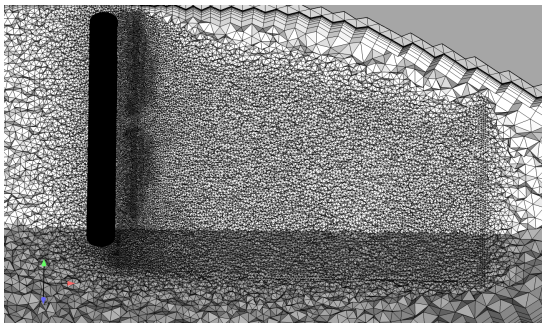

(b) Baseline Mesh

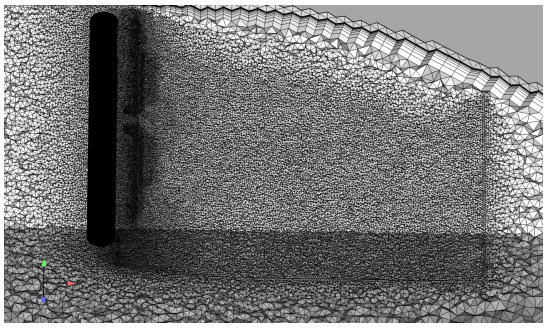

(c) Refined Mesh

Figure 5.2 Mesh Refinement on the Element Sizes in the Wake behind the Drop Tube.

5.2.2 Effect of Slot in Drop Tube on Particle Delivery

It was anticipated that the pressure relief slot on the drop tube would encourage a more uniform flow for the droplets; but does it enhance the flow enough to warrant the additional complexity? The slot and inner tube were removed from the drop tube design

to determine the effect of the slot on the flow inside the drop tube and its subsequent effect on the droplet trajectories. First, the magnitude of the fluctuations inside the drop tube is examined to determine behavior of the flow. Figure 5.3 shows that the vertical flow inside the drop tube suffers from fluctuations near the exit that might adversely affect the droplet trajectories.

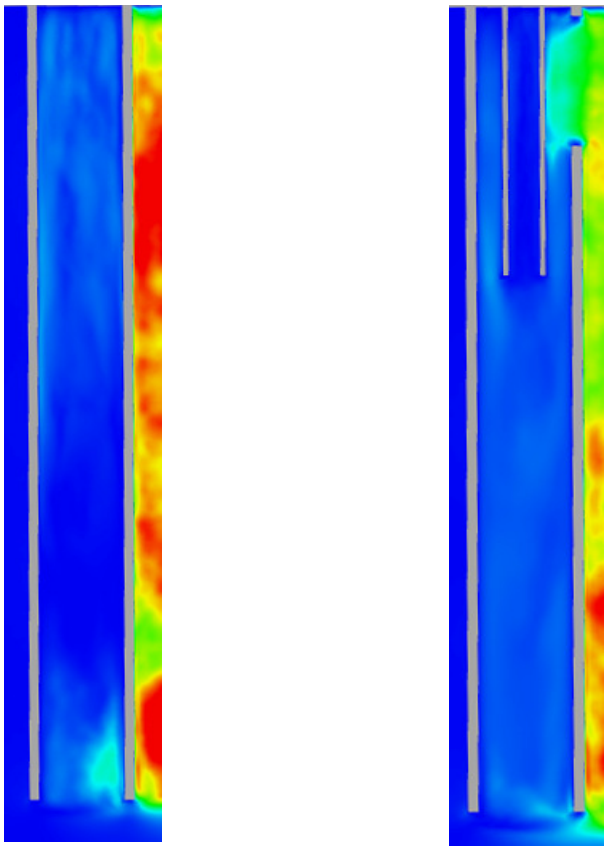

(a) Drop Tube (b) Slotted Drop Tube

Figure 5.3 Transverse Turbulent Component Parallel to the Wake.

Ultimately, the most important function of the drop tube is introducing droplets into the flow in the wind tunnel. Repeatable droplet impact on the test specimen is the benchmark for each drop tube design. Therefore, the scatter of droplet trajectories in the test section is one way to assess the performance of each drop tube design. Figure 5.4 displays the scattering of droplets in the test section for the configuration with the slot and the inner tube and an unmodified single tube. The scatter plots are sampled at the middle of the test section and include all droplets that cross the middle of the test section over a sample time of 0.152*s*. Forty temporal samples were taken in each test case. Examination of the scatter plot shows that the non-uniform flow inside the drop tube does

not prohibit droplets from exiting the drop tube. However, the droplet trajectories do suffer from more left to right scatter in the test section than if there is no pressure relief slot or inner tube. As will be seen in all of the trajectory plots for the circular cross section drop tubes, the trajectories are deflected upward relative to the exit of the drop tube. This is a result of the mean flow in the wake behind the cylinder. The fluctuations in the wake are responsible for the side-to-side and bottom-to-top variability in the trajectories.

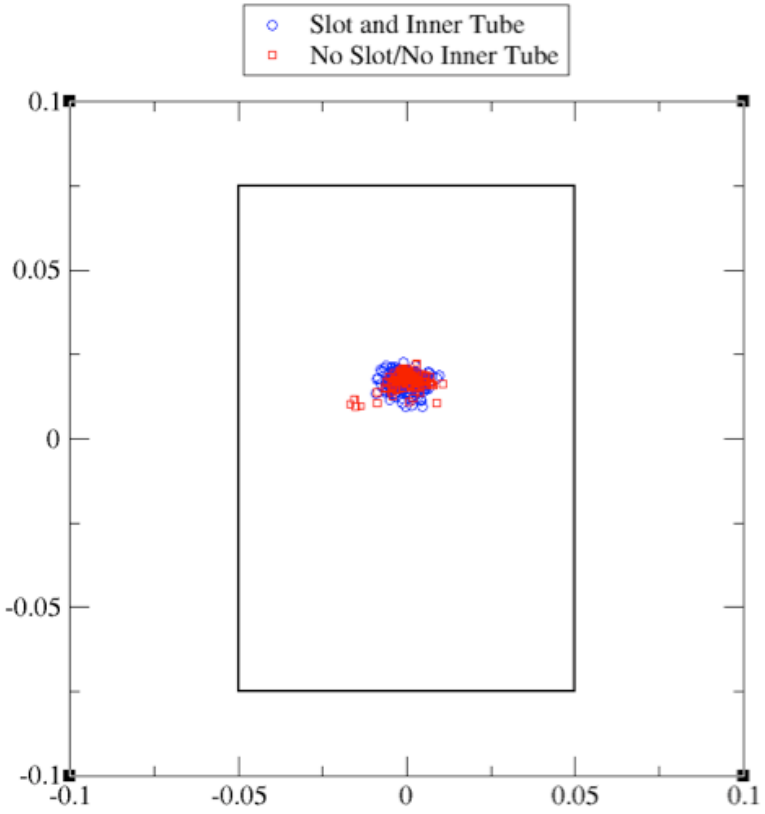

Figure 5.4 Droplet Scatter of the Non-Slotted and Slotted Drop Tube.

Examination of droplet paths inside the drop tube reveals more information about the effects of the slot. The droplets are colored by their velocities in figure 5.5 to provide insight to instantaneous flow patterns inside the drop tube. The droplets inside the drop

tube with no slot fall unaffected for some length until adverse vertical air flow reduces the droplet velocities, alters their trajectories, and increases the scattering of droplets in the tube as shown in figure 5.5. Inspection of the slotted drop tube reveals that the velocity of the droplets increases as they fall through the drop tube. The swirl of droplets in the drop tube is evidence of residual effects of flow around the inner tube. The dispersion of droplets created by swirling flow does not affect the scatter of droplets as much as the dispersion caused by the adverse flow.

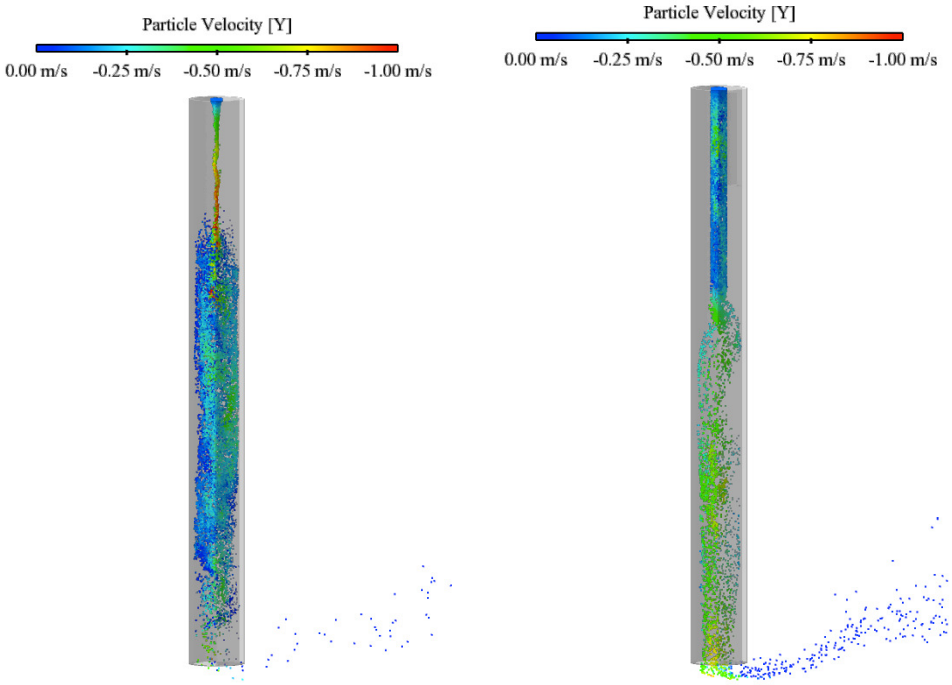

(a) Drop Tube (B) Slotted Drop Tube

Figure 5.5 Instantaneous Droplets Inside the Drop Tube at 1.52*s* after Initial Release.

The rate of droplets exiting the drop tube can also be used to assess the effect of the slot on the droplet trajectories. In both cases, several droplets impact the inside of the drop tube and fail to exit the tube. Figure 5.6 displays droplet impact locations inside the

drop tube for both the (a) drop tube and (b) slotted drop tube. The surface elements of the drop tube are colored by the mean of the droplet mass flux through the tube wall. Figure 5.6 shows that droplets in the slotted drop tube are less likely to impact the walls of the drop tube. It was assumed that, when a droplet impacts a wall, it is instantaneously removed from the domain. This assumption ignores the possible accretion of ice inside the drop tube over time if droplet impacts are frequent. Eventually, this accretion may block all flow from exiting the drop tube preventing any droplets from exiting the tube.

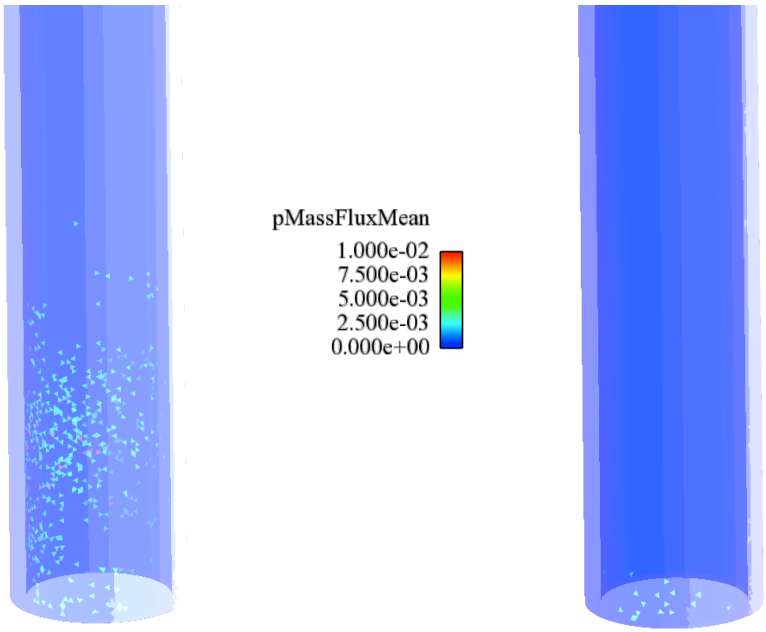

(a) Drop Tube (b) Slotted Drop Tube

Figure 5.6 Comparison of Droplet Impacts Inside the Drop Tubes over 0.152*s*.

Another way to assess the quality of flow in the drop tube is to plot the scatter of droplets at the exit of the drop tube. Figure 5.7 displays this scattering of droplets that exit the different drop tube designs. The droplets in the unmodified tube are displayed by red symbols and those in the slotted drop tube are displayed by blue symbols. The plot

tracks all of the droplets that cross the exit plane of the drop tube over a time interval of 0.152 seconds.

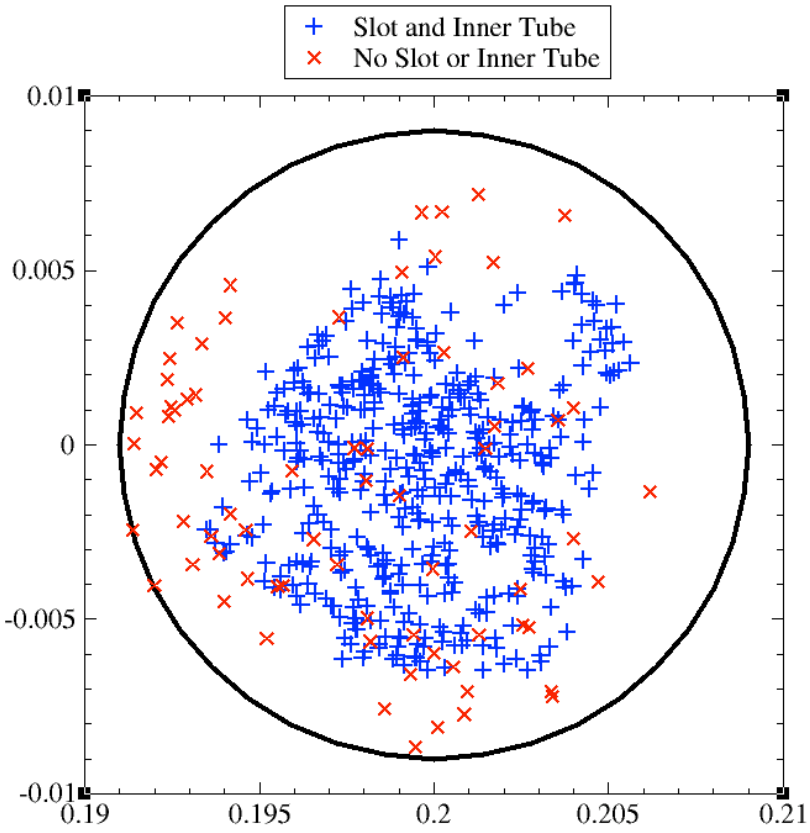

Figure 5.7 Comparison of Droplets Exiting the Drop Tube over 0.152*s*.

Figures 5.6 and 5.7 show that, in the slotted drop tube, significantly more droplets exit the drop tube and fewer impact the inside of the drop tube. The scatter plots show that 116 droplets exit the drop tube and 491 droplets exit the slotted drop tube during the specified time interval. Thus, the slotted drop tube increases the rate of droplets successfully exiting the drop tube during this time interval and improves the scattering of droplet trajectories in the test section. Although these plots show that significantly more droplets pass through the drop tube exit over this time period; the disparity between the two designs may not be as significant as the sample period increases. The initial sample

only proves that the slotted drop tube emits droplets at a greater rate than the drop tube with no slot.

5.2.3 Effect of Slot Dimensions on Particle Delivery

One possible modification to the drop tube design is to reduce the size of the pressure relief slot. Presumably, changes to the slot will affect the flow moving through the drop tube and may alter the trajectories of the droplets. Figure 5.8 shows the instantaneous droplet positions and scattering of droplets in the test section. The vertical deflection and scattering of the droplets in the test section are the products of the cylindrical cross-section drop tube design. In this case, there are several more outlying particles scattered across the width of the test section in comparison with the trajectories for the larger slot.

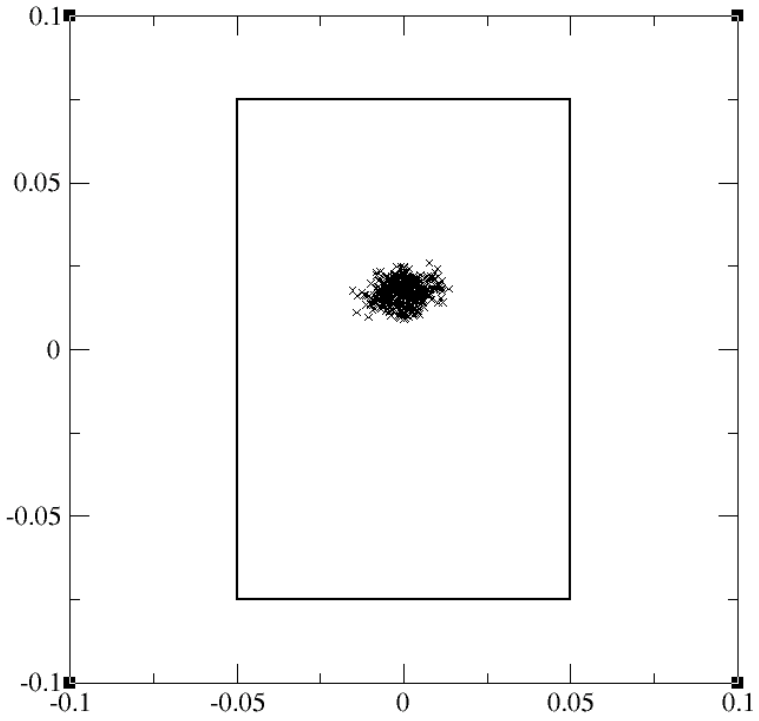

Figure 5.8 Scatter of Droplets Inserted Through the Drop Tube with Smaller Slot.

Inspection of the instantaneous droplet positions inside the drop tube, displayed in figure 5.9, shows that swirl in the flow affects the droplets as in the drop tube with the larger slot. However, for the smaller slot, the effect of the swirling flow does not affect the droplet trajectories until the droplets travel further in the drop tube. Also, the smaller slot increases the flow velocity in the drop tube, thus increasing the droplet velocities.

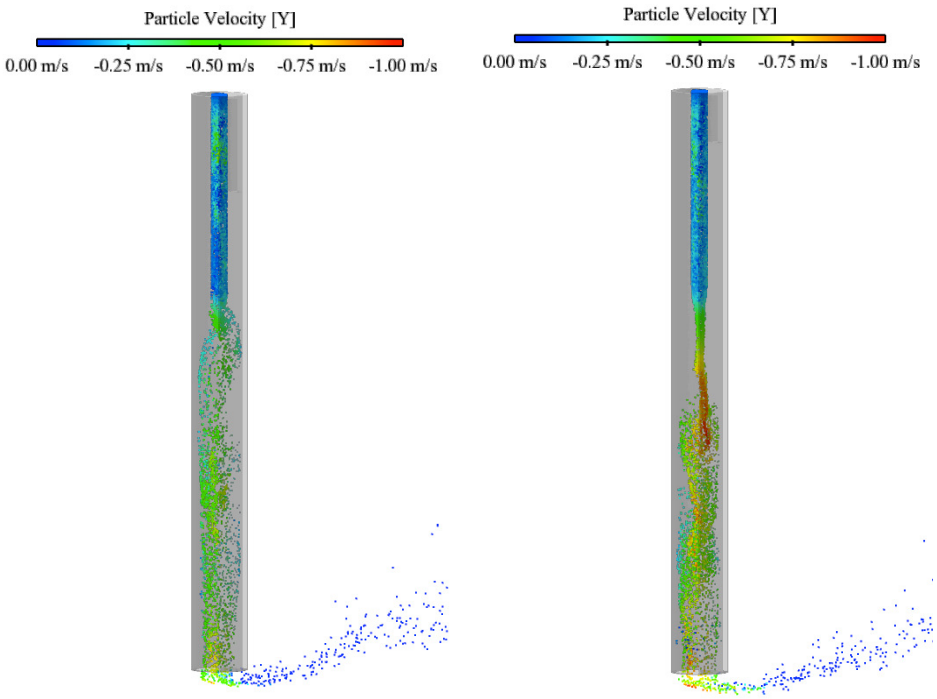

Figure 5.9 Left: Drop Tube with Slot and Right: Drop Tube with ½ Size Slot.

5.2.4 Effect of Turbulent Wake on Droplet Trajectories

It is apparent that the wake of the drop tube has a significant impact on the droplet trajectories. One way to quantitatively assess the effects of the wake is through the fluctuations, i.e., the root mean square (RMS) of the deviation between the instantaneous velocity and the mean velocity. Schlichting [38] contends that typical investigations of mean flow values are usually sufficient, but examination of the turbulent components reveals the full motion of the flow. Adopting Schlichting's nomenclature, the RMS of the x component is referred to as the longitudinal turbulent component, the y component as the transverse component parallel to the wake, and the z component as the transverse component at a right angle to the wake. Examining the transverse turbulent component at

right angles to the wake provides some insight into motion of the flow and the effects of mesh refinement on the simulated fluctuations.

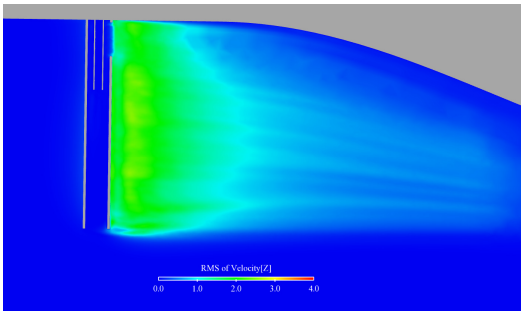

(a) Coarse Mesh

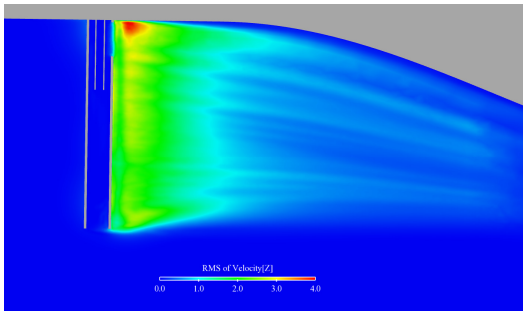

(b) Baseline Mesh

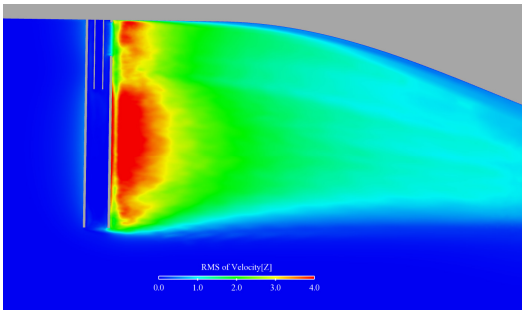

(c) Refined Mesh

Figure 5.10 RMS Values of the Transverse Turbulent Component at Right Angles to the Wake in the Mid-Plane of the Wind Tunnel.

Inspection of figure 5.10 shows a significant change in the turbulent intensity as the mesh is refined. The images in figure 5.10 display the magnitudes of transverse turbulent components at the mid-plane of the wind tunnel. Over 200 samples were used to calculate the mean and RMS flow values for each of these test cases. The most refined mesh exhibits strong turbulent fluctuations behind the drop tube, but the fluctuation strength decreases by 25% as the mesh is coarsened.

5.2.5 Impact of Mesh Refinement on Droplet Trajectories

The scatter of droplets trajectories in the test section for each of the meshes examined in the refinement study is shown in Figure 5.11. As before, the droplets were released randomly across the opening of the inner tube at a rate of $0.56 kg/s/m^2$. As the flow passes through the converging section, it experiences longitudinal acceleration and a corresponding decrease in cross-sectional area, which focuses the droplet paths. Figures 5.11(a), 5.11(b), and 5.11(c) display the scatter of particles calculated from 40 instantaneous samples over $0.151 s$ of simulation.

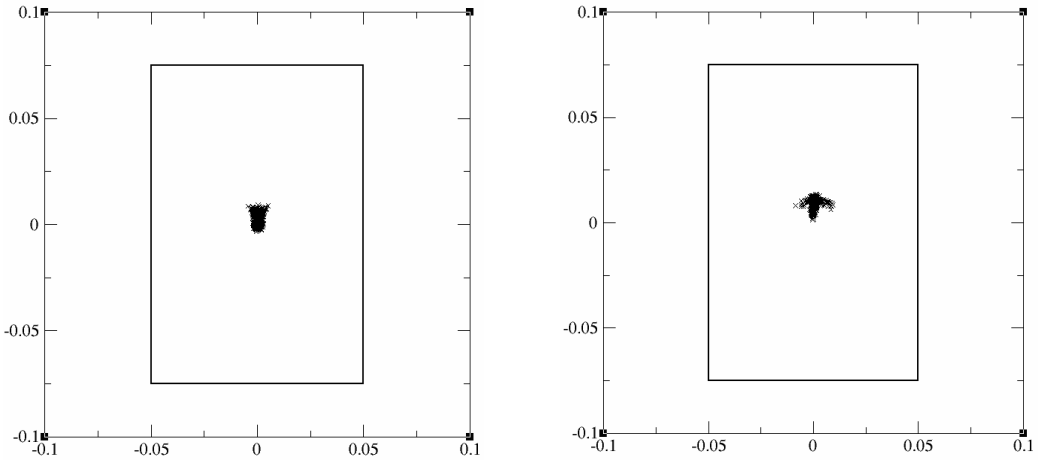

(a)Coarse Mesh (b) Baseline Mesh

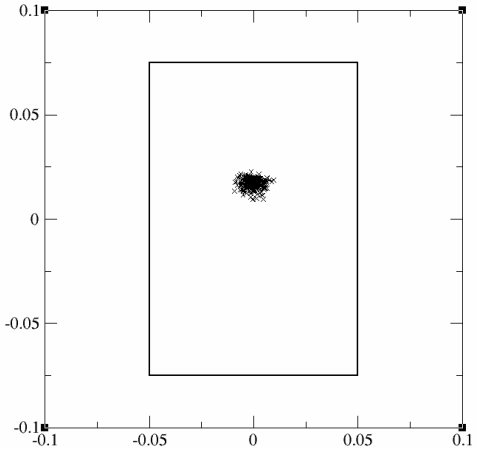

(c) Refined Mesh

Figure 5.11 Comparison of Droplet Scatter in Slotted Drop Tube.

Examination of Figure 5.11 shows that the cylindrical drop tube design exhibits a considerable scatter across the width of the test section. The scatter increases as the mesh is refined. This is due to the weakened fluctuations caused by insufficient spatial resolution in the coarser meshes. The scatter plots also show that the droplet trajectories are deflected above the centerline of the wind tunnel when released from cylindrical drop tubes. The upward deflection is also increased as the mesh is refined.

5.3 Alternate Drop Tube Designs

The cylindrical cross-section drop tube design tends to scatter the droplets, due to the fluctuating velocity components, as well as deflect them upwards, due to the mean flow. Presumably, less scatter and therefore more reliable droplet trajectories would be the result of employing other cross-sections for the drop tube that produce less turbulence in the wake. The intensity of transverse turbulent fluctuations at right angles to the wake, as shown in Figure 5.12, may be employed to determine the cross-section that produces the least turbulence downstream. The cylindrical cross-section drop tube shows a strong, very active turbulent wake. Presumably, if the drop tube were made more streamlined, the turbulent intensity in the wake would be reduced.

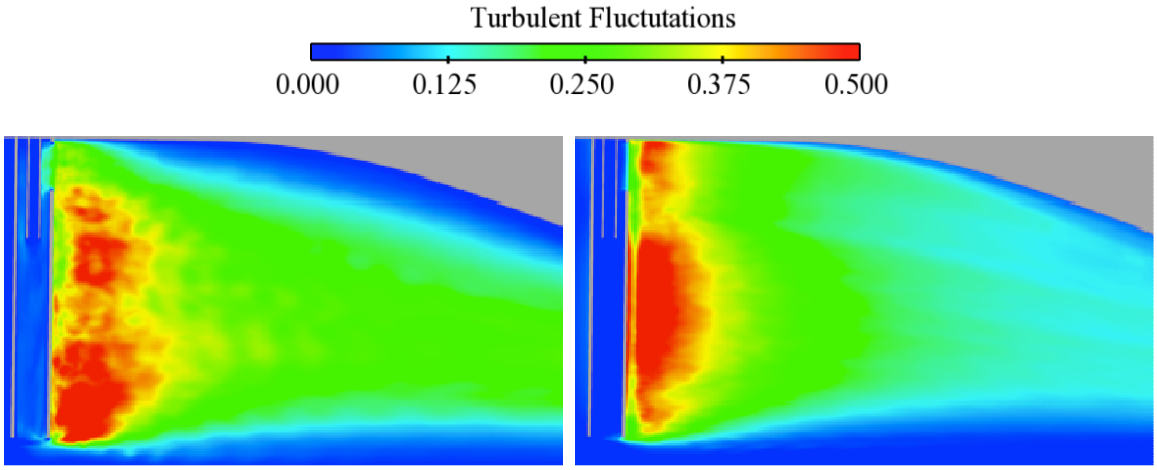

(a) Cylindrical Cross-Section. Left: Right Angle to the Wake. Right: Parallel to the Wake.

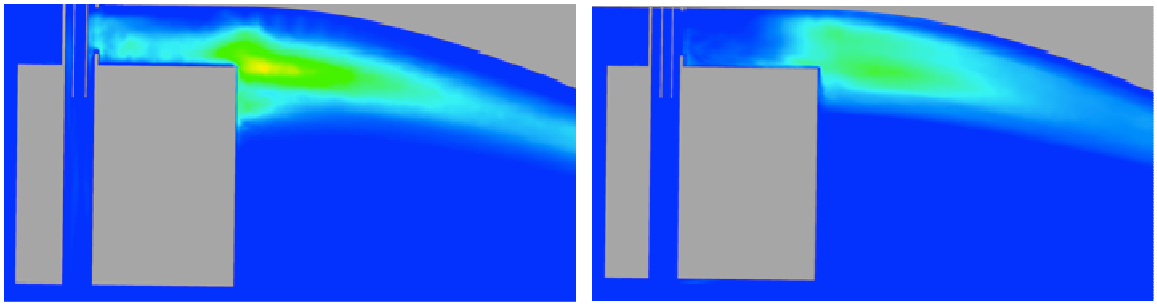

(b) NACA0020 Cross-Section. Left: Right Angle to the Wake. Right: Parallel to the Wake.

Figure 5.12 Transverse Turbulent Fluctuations for Different Airfoil Cross Sections.

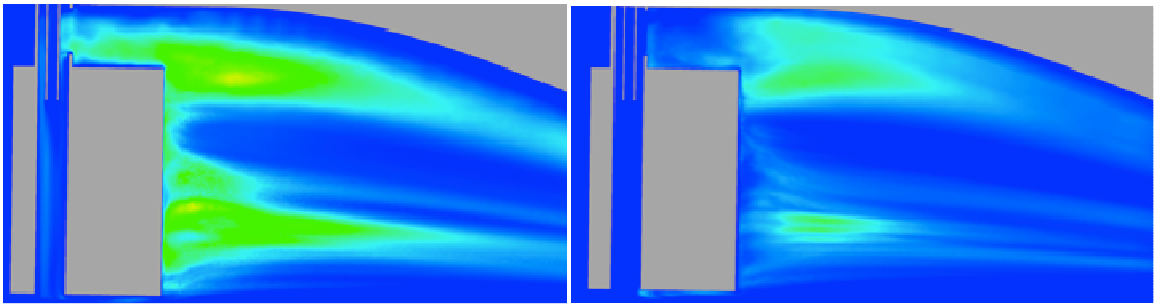

(c) NACA0030 Cross-Section. Left: Right Angle to the Wake. Right: Parallel to the Wake.

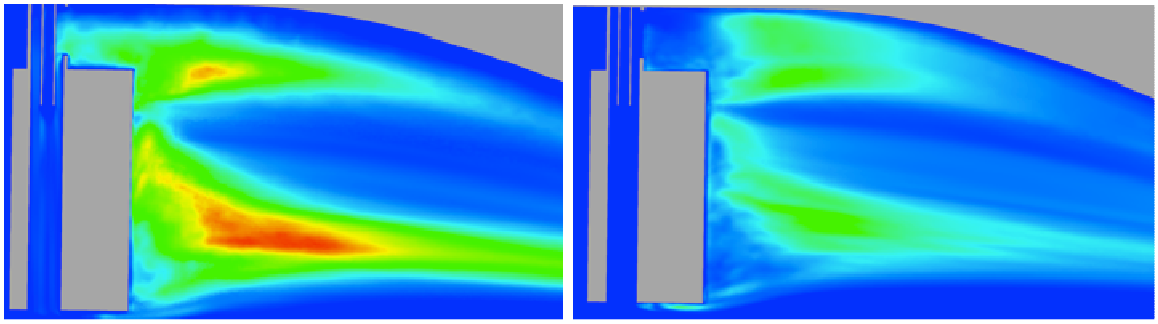

(d) NACA0040 Cross-Section. Left: Right Angle to the Wake. Right: Parallel to the Wake.

Figure 5.12 (continued)

Not surprisingly, each of the drop tubes with airfoil cross-sections produces significantly smaller regions of high intensity turbulent flow than the cylindrical drop tube. The NACA0020 cross-section nearly eliminates all of the turbulence near the exit of the drop tube, which has more impact on the droplets. The other airfoil cross-section drop tubes produce higher turbulence levels in this region.

However, the most important feature of the drop tube design is its effect on the droplet trajectories. The droplet scatter in the test section is shown in figure 5.15 for the

cylinder cross-sections and each of the drop tubes with airfoil cross-sections. Examination of figure 5.15 reveals that all of the drop tubes with airfoil cross-sections produce droplet trajectories with minimal scatter in the test section.

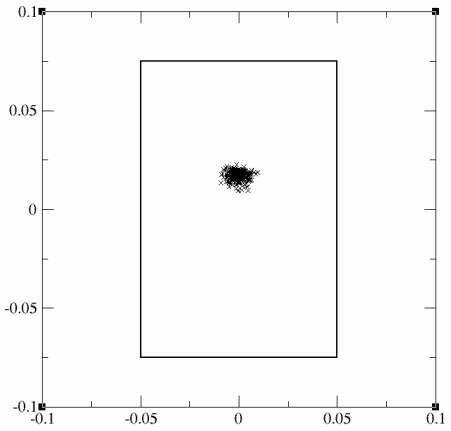

(a) Cylindrical Cross-Section

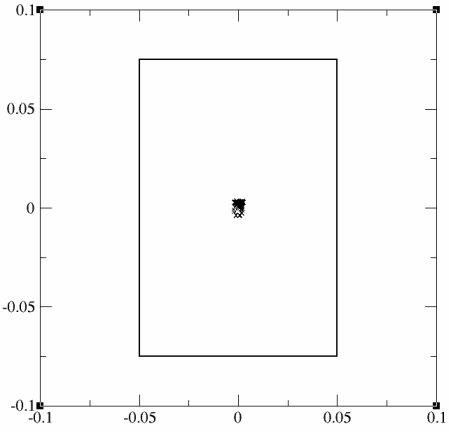

(b) NACA0020 Cross Section

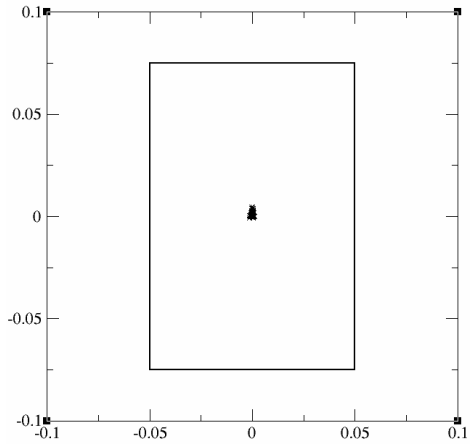

(c) NACA0030 Cross Section

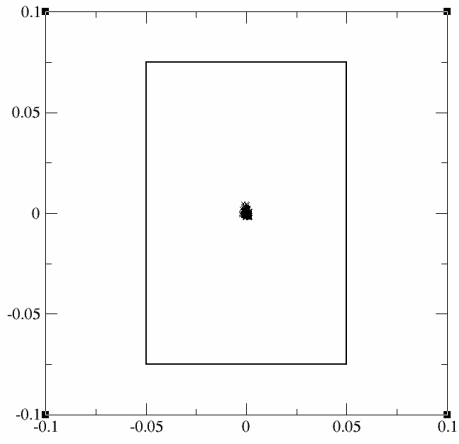

(d) NACA0040 Cross Section

Figure 5.13 Scatter Plots of Droplets Passing through the Test Section over 0.152*s*.

Examination of figure 5.13 shows that all of the airfoil cross-sections produce less scatter in the droplet trajectories than the cylindrical cross section. The unpredictable nature of the cylindrical drop tubes is probable cause for using one of the hybrid drop

tube designs. Figures 5.11 and 5.12 show that the NACA0020 cross-section drop tubes produce the least amount of turbulence. The length of the NACA0020 airfoil required to maintain a thickness of 24*mm* is quite large though, and could overly restrict the flow in the wind tunnel. The NACA0030 drop tube shows a tighter scattering of particles in figure 5.13 part (c).

CHAPTER VI

CONCLUSIONS

The geometric design of the droplet delivery device can significantly alter the flow in the wind tunnel. In addition, the turbulent wake behind the drop tube can influence the trajectories of the water droplets. Limiting the variation in droplet trajectories is critical to ensuring that the droplets will impact a test specimen.

The findings of this research are summarized below:

1. It was demonstrated that droplets released through a cylindrical drop tube exit the tube and enter the flow in the wind tunnel. Adding a pressure relief slot and inner tube to the drop tube design significantly improves the rate of particle exits from the drop tube and reduces the scatter of the droplet trajectories. However, the cylindrical drop tube creates a strong turbulent wake that tends to deflect the droplets off of their course down the center of the test section.

2. Adding an airfoil shaped collar to the lower portion of the drop tube reduces the intensity of the turbulent wake behind the drop tube and reduces the variability of droplet trajectories in the test section. This reduced wake intensity produces a significantly smaller scattering of droplets downstream. All of the airfoil shaped cross sections significantly decreased the scatter in the droplet trajectories. The drop tube with the NACA0020 cross section significantly reduced the turbulent intensity in the wake behind the drop tube, but did not produce the most reliable droplet trajectories. The NACA0030 cross section produced the smallest scattering of droplets in the test section.

Figure 6.1 displays the improvement of the airfoil collars on droplet trajectories in the test section. The droplets released from the slotted cylindrical drop tube are displayed by the blue symbols and the droplets released from the NACA0020 airfoil-shaped drop tube are displayed in red. Each of the airfoil-shaped drop tubes produce results similar to the NACA0020 shown below. Figure 6.1 shows that the effect of the mean flow in the wake downstream of the cylindrical drop tube is to deflect the droplets upward. The droplets released from the airfoil shaped drop tubes pass through the center of the test section with only small deflections.

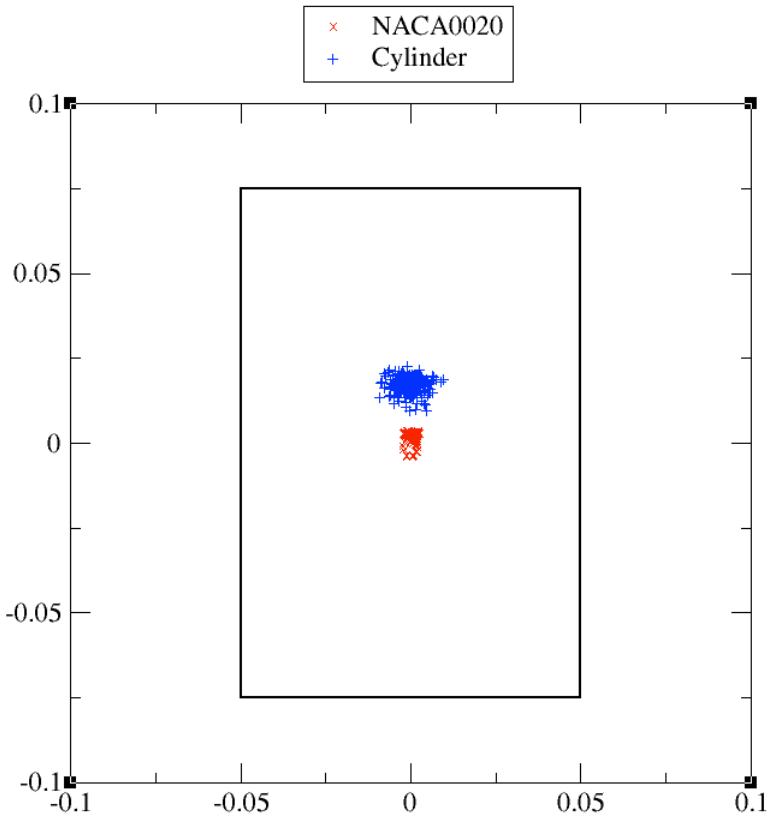

Figure 6.1 Comparison of Droplet Scatter in the Test Section over 0.152*s*.

The airfoil shaped drop tubes emit droplets in a more consistent pattern than the cylindrical shaped drop tube. Figures 5.12 and 5.13 show that the NACA0020 and

NACA0030 shapes produce a more consistent droplet scatter than the NACA0040 by reducing the turbulent fluctuations in the flow. Figure 6.2 compares the droplet scatter from the NACA0020 and NACA0030 shaped drop tubes. Overall, the droplets emitted from the NACA0030 drop tube exhibit less upward deflection and less horizontal scattering than the droplets emitted from the NACA0020 drop tube. For a fixed thickness, the chord length of the NACA0020 is significantly larger than the chord length of the NACA0030 and may be the root cause of inferior performance in terms of droplet scatter.

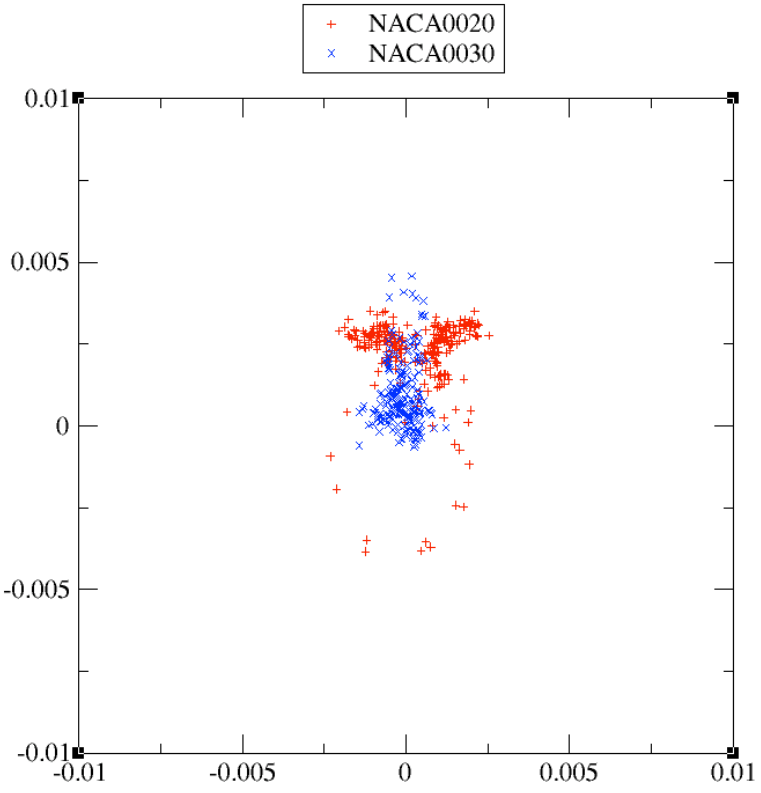

Figure 6.2 Comparison of Droplet Scatter in the Test Section over 0.152*s*.

For the conditions of interest, the best performing drop tube design includes a pressure relief slot, an inner tube, and a NACA0030-shaped collar. While this design is

not the best in terms of the level of turbulence in the wake of the drop tube, it does produce the tightest pattern of droplet trajectories in the test section.

REFERENCES

[1] U.S. Department of Transportation, Federal Aviation Administration, "Federal Aviation Regulations Part 23, Subpart F, Safety Equipment, Ice Protection," 58 FR 18977, Apr. 9, 1993.

[2] Hill E., Roy M., Botura G., Riley J., Dumunt C., Pullin D., Uppiluri S., Broeren A., Selig M., and Anderson D. "Investigations of Performance of Pneumatic Deicing Boots, Surface Ice Detectors, and Scaling of Intercycle Ice." DOT/FAA AR-06/48, 2006.

[3] U.S. Department of Transportation, National Transportation Safety Board,"In-Flight Icing Encounter and Loss Of Control American Eagle Flight 4184, Avions de Transport Regional (ATR) Model 72-212, Roselawn, Indiana October 31,1994, Volume 1 Safety Board Report," NTSB/AAR-96/01, 1996.

[4] U.S. Department of Transportation, National Transportation Safety Board,"In-Flight Icing Encounter and Uncontrolled Collision with Terrain Comair Flight 3272 Embraer EMB-120RT, N265CA Monroe, Michigan January 9, 1997,"NTSB/AAR-98/04, 1999.

[5] Raps, D., "Getting Started Anyway…," Email to Thompson, D., and Hutchings, K., Feb. 9, 2009.

[6] Gaither, J., Marcum, D., and Mitchell, B., "SolidMesh: A Solid Modeling Approach to Unstructured Grid Generation," *Proceedings of the 7th International Conference on Numerical Grid Generation in Computational Field Simulations*. ISGG. Whistler, BC, 2000.

[7] Luke, E., Tong, X., Wu, J., Tang, L., and Cinnella, P., "A Step Towards 'Shape Shifting' Algorithms: Reacting Flow Simulations using Generalized Grids," AIAA Paper 2001-0897, 2001.

[8] National Aeronautics and Space Administration, *NASA Glenn Research Center*, 2008, URL: http://facilities.grc.nasa.gov/irt/ [cited 22 July 2010].

[9] The Boeing Company, *Boeing Technology Services-Aerodynamics*, 2010, URL: http://www.boeing.com/commercial/techsvcs/boeingtech/bts_aerof.html [cited 22 July 2010].

[10] Italian Aerospace Research Center, *Extreme Icing Environment Focused Research Project*, 2007, URL: http://extice.cira.it/partners/extice-main-facilities/cira-iwt [cited 22 July 2010].

[11] Canadian National Research Council, *NRC Institute for Aerospace Research*, 2009, URL: http://www.nrc-cnrc.gc.ca/eng/facilities/iar/altitude-icing.htm [cited 22 July 2010].

[12] Hirsh, C., *Numerical Computation of Internal and External Flows*, 2nd ed., Butterworth-Heinemann, Oxford, 2007, pp. 83-94.

[13] Spalart, P., Jou, W.-H., Strelets, M., and Allmaras, S., "Comments on the Feasibility of LES for Wings and on a Hybrid RANS/LES Approach," *Advances in DNS/LES,* edited by C. Liu and Z. Liu, Greydon Press, Columbus, OH, 1997.

[14] Breuer, M., "Large Eddy Simulation of the Subcritical Flow Past a Circular Cylinder: Numerical and Modeling Aspects," *International Journal for Numerical Methods in Fluids*, Vol. 28, No. 9, 1998, pp. 1281-1302.

[15] Nichols, R. and Nelson, C., "Application of Hybrid RANS/LES Turbulence Models," AIAA 2003-0083, 2003.

[16] Tutar, M., and Holdo, A., "Computational Modeling of Flow around a Circular Cylinder in Sub-Critical Flow Regime with Various Turbulence Models," *International Journal for Numerical Methods in Fluids*, Vol. 35, No. 7, 2001, pp. 763-784.

[17] Celik, I., and Shaffer, F., "Long Time-Averaged Solutions of Turbulent Flow Past a Circular Cylinder," *Journal of Wind Engineering and Industrial Aerodynamics*, Vol. 56, No. 2-3, 1995, pp. 185-212.

[18] Smagorinsky, J., "General Circulation Experiments with the Primitive Equations I. The Basic Experiment," *Monthly Weather Review*, Vol. 91, No. 3, 1963, pp. 99-164.

[19] Spalart, P., and Allmaras, S., "A One-Equation Turbulence Model for Aerodynamic Flows," AIAA Paper 92-0439, 1992.

[20] Travin, A., Shur, M., Strelets, M., and Spalart, P., "Detached-Eddy Simulations Past a Circular Cylinder," *Flow, Turbulence and Combustion*, Vol. 63 No. 1-4, 1999, pp. 293–313.

[21] Roy, C., DeChant, L., Payne, J., and Blottner, F., "Bluff-Body Flow Simulations Using Hybrid RANS/LES," AIAA Paper 2003-3889, 2003.

[22] Menter, F., "Two-Equation Eddy Viscosity Turbulence Models for Engineering Applications," *AIAA Journal*, Vol. 32, No. 8, pp. 1657-1659.

[23] Bloor, S. "The Transition to Turbulence in the Wake of a Circular Cylinder," *Journal of Fluid Mechanics*, Vol. 19, No. 2, 1963, pp. 290-304.

[24] Holloway, D., Walters, D., and Leylek, J., "Prediction of Unsteady, Separated Boundary Layer Over a Blunt Body for Laminar, Turbulent, and Transitional Flow," *International Journal for Numerical Methods in Fluids*, Vol. 45, No. 12, 2004, pp. 1291-1315.

[25] Breuer, M., "A Challenging Test Case for Large Eddy Simulation: High Reynolds Number Circular Cylinder Flow," *International Journal of Heat and Fluid Flow*, Vol. 21, No., 5, 2000, pp. 648-654.

[26] Luke E., Tong X. Wu J., and Cinnella P., "CHEM 3: A Finite-Rate Viscous Chemistry Solver – The User Guide," Jan. 2009.

[27] Zhang, Z. and Chen, Q., "Comparison of the Eulerian and Lagrangian methods for predicting particle transport in enclosed spaces," *Atmospheric Environment*, Vol. 41, No. 25, 2007, pp. 5236-5248.

[28] Premoze S., Tasdizen T., Bigler J., Lefohn A., and Whitaker R., "Particle-Based Simulation of Fluids," *Eurographics*, Vol. 22, No. 3, 2003, pp. 401-410.

[29] Knupp P., "Remarks on Mesh Quality," AIAA Paper 2008-933, 2008.

[30] Mavriplis D., Vassberg J., Tinoco E., Mani M., Brodersen O., Eisfeld B., Wahls R., Morrison J., Zickuhr T., and Levy D., "Grid Quality and Resolution Issues from the Drag Prediction Workshop Series," AIAA Paper 2008-930, 2008.

[31] Luke E., Hebert S., and Thompson D., "Theoretical and Practical Evaluation of Solver-Specific Mesh Quality," AIAA Paper 2008-934, 2008.

[32] Salas M., "Some Observations on Grid Convergence," *Computers and Fluids*, Vol. 35, No. 7, 2006, pp. 688-692.

[33] Thomas J., Diskin B., and Rumsey C., "Towards Verification of Unstructured-Grid Solvers," AIAA Paper 2008-666, 2008.

[34] Marcum, D., and Weatherill, N., "Unstructured Grid Generation using Iterative Point Insertion and Local Reconnection," *AIAA Journal*, Vol. 33, No. 9, 1995, pp. 1619-1625.

[35] Balay, S., Buschelman, K., Eijkhout, V., Gropp, W., Kaushik D., Knepley, M., Curfman-McInnes, L., Smith, B., and Zhang, H., "PETSc Users Manual," Argonne National Laboratory, ANL-95/11, 2008.

[36] Saad, Y., and Schultz, M., "GMRES: A Generalized Minimal Residual Algorithm for Solving Nonsymmetric Linear Systems," *SIAM Journal of Scientific Statistics and Computers,* Vol. 7, No. 3, 1986, pp. 856-869.

[37] Fey, U., Konig, M., and Eckelman, H., "A New Strouhal-Reynolds-Number Relationship for the Circular Cylinder in the Range 47< Re< 2× 105," *Physics of Fluids*, Vol. 10, No. 7, 1998, pp. 1547-1549.

[38] Schlicting, H., *Boundary Layer Theory*. 5th ed., McGraw-Hill, New York, 1979, pp. 510-514.

APPENDIX A

INPUT VARS FILE FOR TIME ACCURATE FLOW SIMULATIONS WITH LAGRANGIAN PARTICLE TRACKING

```
loadModule: Particle
{
//------Icing Tunnel with Lagrangian Particle Traces-------
//-----------Grid file and Boundary Conditions------------
grid_file_info: <file_type = VOG,Lref = 1.0m>
boundary_conditions: <
//Transient BC
//
//Inflow = isentropicInflow(p0=1.0atm,T0=270.144K,k=0.3518,w=7735),
//OuterTube = viscousWall(adiabatic),
//Outflow = fixedMassOutflow(mdot=1.2967kg/sec),
//Tunnel =  viscousWall(adiabatic),
//InnerTube =  viscousWall(adiabatic),
//Opening =  viscousWall(adiabatic),
//Spray = viscousWall(adiabatic),
//Extension =  viscousWall(adiabatic)
//>
//boundary_conditions: <
//Particle Trace BC
//
Inflow = isentropicInflow(p0=1.0atm,T0=270.144K,k=0.3518,w=7735),
OuterTube = viscousWall(adiabatic,stickwall),
Outflow = fixedMassOutflow(mdot=1.2967kg/sec),
Tunnel = viscousWall(adiabatic,stickwall),
InnerTube = viscousWall(adiabatic,stickwall),
Opening = viscousWall(adiabatic,stickwall),
Extension = viscousWall(adiabatic,stickwall),
Spray = reflecting(particleType=water,
                                                particleSizes=60e-6m,
                                                particleSpeed=0.11m/s,
                                                particleMassFlux=0.56kg/s/m/m,
                                                particleInjectDensity=5e5)
>

//-----------Initial Conditions--------------------------
initialConditions: <p=1.0atm,T=268.0K,u=0.0m/s>
p0:1atm
//interpolateInitialConditions: output/put.0_Inner0020_ext

//--------Chem and Turb Model Setup-----------------------
chemistry_model: air_1s0r
transport_model: sutherland
turbulence_model: SST
multi_scale: LES
```

```
//--------Numerical Algorithm Setup-----------------------
plot_interval: 7.61e-3 sec

print_freq: 25
plot_modulo: 0
plot_freq: 5
restart_freq: 50
restart_modulo: 0
stop_iter: 1000


// Setting up the code for steady stat convergence
// number of newton iterations, must be 1 or greater
newton_iter: 6

// number of gauss seidel iterations used in linear system solution
// 0 will do local block jacobi
gauss_seidel_iter: 5

// time integration method, options are: euler, second_order
// euler is typically used to relax to steady state
time_integration: time_accurate

//Gravity
gravity: <g=[0,-9.81,0],rhoref=1.317>

// Maximum cfl, this enables local timestepping used for steady state
// computations
cflmax:  100000

// Underrelaxation parameter that controls how much the solution is allowed to
// change in any given timestep (Also a local timestep control)
urelax: 1.0

// The maximum timestep
dtmax:  7.61e-4

// Use numerical jacobian instead of Roe matrix
inviscid_fjmat: numerical


// Use Venkat's limiter
limiter: venkatakrishnan
```

```
// This option turns on the petsc solver for the linear system.
// Generally this makes timesteps much slower, but may allow convergence
// with fewer timesteps.
fluidLinearSolver: petsc

//Preconditioning
Minf: 0.9

// Output the turbulent viscosity as well as other flow variables
plot_output: r,v,P

//particle time step
p_dtmax: 7.61e-4
particle_model: water
}
```